J. Mech. Phys. Solids 159 (2022) 104713

Contents lists available at ScienceDirect

Journal of the Mechanics and Physics of Solids

journal homepage: www.elsevier.com/locate/jmps

Adhesion of beams with subsurface elastic heterogeneity

Aoyi Luo, Kevin T. Turner *

Department of Mechanical Engineering and Applied Mechanics, University of Pennsylvania, Philadelphia, PA 19104-6315, USA

ARTICLE INFO

Keywords:
Adhesion
Heterogeneous structure
Subsurface stiffness modulation
Double cantilever beam
Interface fracture

ABSTRACT

Beam-like structures with enhanced and selective adhesion as well as low stiffness are of interest for applications such as microtransfer printing processes and soft robotic grasping devices. The stiffness and adhesion of compliant beams can be altered through the inclusion of structured stiff insets that alter the mechanical response and stress distribution at the adhered interface. Here, the adhesion behavior of compliant beams with embedded stiff insets below the surface are investigated. The length of inset and the spacing of the insets relative to the beam height are key parameters that control the adhesion behavior. The inclusion of a stiff inset increases the effective adhesion of the beam, but the maximum adhesion enhancement is only realized when the inset exceeds a critical inset length. The spacing between the insets plays a key role as well and inset spacings $<\sim$1.5 times height of the beam result in interactions between insets that can be exploited to increase the effective adhesion. Overall, this work provides an understanding of how subsurface elastic heterogeneity affects delamination behavior of beams and provides guidance for the design of heterogeneous beams containing insets to realize controlled adhesion and bending rigidity.

1. Introduction

Materials with elastic heterogeneity are common in nature and this heterogeneity can impart unique mechanical properties, including improved fracture toughness and enhanced adhesion. Teeth, bone, and shells of mollusks and turtles are all examples of materials in which significant elastic heterogeneity contributes to high fracture toughness and damage tolerance (Studart, 2013). Furthermore, insects such as coccinella septempunctata (ladybugs) and carausius morosus (stick insects) leverage elastic heterogeneity, in the form of a gradient in elastic modulus, to achieve high and reversible adhesion to a broad range of surfaces (Peisker et al., 2013; Scholz et al., 2008). These examples from nature illustrate the significant potential to exploit elastic heterogeneity to engineer interfaces with unique adhesion and fracture properties.

Engineering materials with elastic heterogeneity to enhance fracture toughness has a long history and is widely exploited in many materials (Dumont et al., 2003; Evans and McMeeking, 1986; Gludovatz et al., 2014; Jiang et al., 2018; Tuan and Brook, 1990; Wang and Xia, 2017; Wang et al., 2019). Compared with fracture toughness, engineering elastic heterogeneity to tune adhesion response has received less attention. In seminal work, Kendall (1975) investigated the peeling of a smooth rubber strip with varying bending rigidity along the direction of delamination. Kendall found that crack propagation at the interface accelerated when a crack propagated from a region of high rigidity to a region of low rigidity and that crack propagation was retarded for the opposite case. The composite strip had significantly higher peel force than strips made entirely of either of the individual components. In more recent

* Corresponding author.
E-mail address: kturner@seas.upenn.edu (K.T. Turner).

https://doi.org/10.1016/j.jmps.2021.104713
Received 9 May 2021; Received in revised form 27 September 2021; Accepted 4 November 2021
Available online 10 November 2021

Nomenclature

a	crack front position
a^*	normalized front position, a/H
a_c	critical crack front position corresponding to the maximum force
b	beam width
C	rotational compliance of the beam
D	bending rigidity of the beam
D^*	normalized bending rigidity of the beam, D/D_0
D^*_{eff}	normalized effective bending rigidity of the heterogeneous beam, D_{eff}/D_0
D_0	bending rigidity of a homogenous beam made of the compliant matrix material
D_{eff}	effective bending rigidity of the heterogeneous beam
E_c	Young's modulus of the compliant matrix
E_s	Young's modulus of the inset
E_c^*	plane strain Young's modulus of the compliant matrix, $E_c/(1-\nu_c^2)$
G	strain energy release rate
G_c	critical strain energy release rate
H	beam height
h	compliant layer thickness underneath the inset
h^*	normalized compliant layer thickness underneath the inset, h/H
L	inset length
L^*	normalized inset length, L/H
L^*_{back}	normalized back transition length (Eq. (5))
L^*_{front}	normalized front transition length (Eq. (4))
L^*_{min}	normalized minimum inset length to realize the bilayer beam's moment (Eq. (6))
L_{all}	beam length
M	applied moment
M^*	normalized critical delamination moment, M_c/M_0
M^*_{avg}	normalized average delamination moment
M^*_f	normalized local maximum delamination moment
M^*_{max}	normalized maximum critical delamination moment
M_0	critical delamination moment of the homogenous beam made of compliant matrix
M_c	critical delamination moment
P	applied force
P^*_{max}	normalized maximum force
P_c	critical delamination force
P_{max}	maximum delamination force
S	inset spacing
S^*	normalized inset spacing, S/H
S^*_{back}	normalized back spacing (Eq. (8))
S^*_{front}	normalized front spacing (Eq. (7))
$S^*_{\min}$	normalized minimum spacing for inset to behave independently (Eq. (9))
U_z	crack opening displacement
U^*_z	normalized crack opening displacement
x	distance along the interface from the crack front
x^*	normalized distance along the interface from the crack front
σ_{zz}	normal stress along the adhered interface
σ^*_{zz}	normalized normal stress along the adhered interface
ν_c	Poisson's ratio of the compliant matrix
ν_s	Poisson's ratio of the inset
θ	angle between two inclined edges of the section
ΔM^*	normalized difference in maximum moment and minimum moment
DCB	double cantilever beam
FE	finite element

work, the adhesion between films with patterned, periodic bending rigidities and a rigid substrate were studied by Xia et al. (2012, 2013) through a combination of theory and experiments. Their work demonstrated that variations in the elastic bending energy can significantly affect the peel force. The peel force fluctuates as the bending rigidity at crack tip changes, and an 8× enhancement of the maximum peel force relative to homogenous tape is achieved when the bending rigidity mismatch between the sections is 8×.

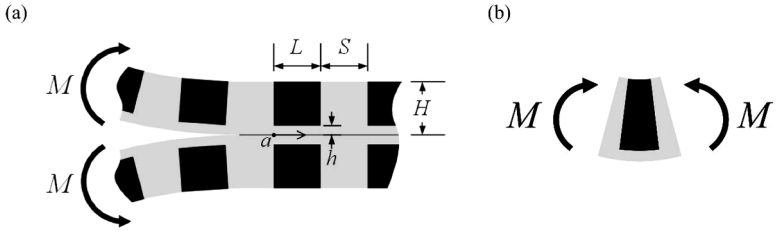

Fig. 1. (a) Schematic of the double cantilever beam (DCB) geometry considered. The black region is stiffer that the gray region, the crack is assumed to propagate from left to right, and the arms of the DCB specimen are loaded in pure bending by applied moments. (b) Schematic of a section containing one period of the structure bends symmetrically when subject to bending moment.

Recently, a kirigami-inspired tape with variation in contact area and bending rigidity was demonstrated to have approximately 100 times enhancement in maximum peel force compared to homogenous tape and also exhibited anisotropy in peeling force in orthogonal peeling directions (Hwang et al., 2018). The adhesion of elastically heterogeneous pillars, which are building blocks for fibrillar surfaces, have also been investigated. The pull-off strength of composite pillars was investigated by Minsky and Turner (2017, 2015) and they demonstrated that the incorporation of a stiff core into a compliant pillar can lead to enhanced adhesion in structures at both the millimeter and micrometer scale. Fischer et al. (2017) and Balijepalli et al. (2017) also investigated adhesion of composite pillars with a soft tip layer and showed that bimaterial structures can offer enhanced adhesion.

The peel and pillar configurations that have been studied previously are important cases but do not provide guidance for designing beam-like structures that exploit elastic heterogeneity for adhesion control. A common soft robotic gripper geometry is a beam structure made of soft elastomer with periodic chamber structures filled with fluid or active materials (Firouzeh and Paik, 2017; Ilievski et al., 2011; Mosadegh et al., 2014; Wang and Ahn, 2017; Zhou et al., 2015). Though widely used for gripping applications through structures like these, strategies to enhance the adhesion of beam-type geometries have not been investigated or optimized. Beyond soft robotics, beam-type structures with a flat continuous surface have been used for temporary attachment in pick-and-place manufacturing processes and microtransfer printing processes for assembling electronic and photonic devices (Kim et al., 2012; Meitl et al., 2006). Our recent work in microtransfer printing has demonstrated that a stamp with a continuous interface is advantageous over a pillar type geometry when transfer printing thin structures (Luo and Turner, 2020), thus motivating the need to control the effective adhesion of continuous interfaces through subsurface effects.

In the example applications discussed above, the beam-type structures need to have not only strong adhesion, but also low bending stiffness so that they can bend easily to long-wavelength flatness variations of the target surface. However, the requirement for both strong adhesion and low stiffness is limited by the widely observed fundamental trade-off between compliance of the system and its adhesion strength (Bartlett et al., 2012; Kendall, 1973). The critical delamination moment M_c of a homogeneous or a layered composite double cantilever beam (DCB) scales with square root of its bending rigidity D (Maugis, 2000):

$$M_c = \sqrt{G_c b D}, \tag{1}$$

where G_c is the critical strain energy release rate, b is the width of the beam. Thus, it is challenging to design beam-like structures for applications such as robotic grippers that have both high compliance to allow for accommodation of non-flatness and high adhesive load capacity.

To achieve enhanced adhesion and overcome this tradeoff, we investigate a beam with segmented subsurface elastic heterogeneity through mechanics-based modeling and experiments in this paper. The adhesion of the beam structure is characterized in terms of a DCB geometry (Fig. 1(a)). Specifically, a DCB comprised of two compliant beams with embedded stiff insets of varying geometry is examined. Importantly, the stiff insets do not extend to the interface thus the role of elastic heterogeneity is examined while retaining a homogenous compliant interface that ensures good contact and uniform work of adhesion. The primary focus in this work is on highly-mismatched cases in which the ratio of moduli between the inset and matrix is on the order of 10^3; this would be typical of a composite system composed of an elastomer matrix and an inset made of a thermoplastic or thermoset polymer.

2. Methods

2.1. Finite element simulations

A moment-loaded symmetric DCB with beam height H that contains repeated inset structures with length L, spacing S, and a thin compliant layer of thickness h between the inset and interface (Fig. 1(a)) was investigated using finite element (FE) analysis. The beams are sufficiently long to avoid edge effects. Linear elastic behavior is assumed in the analysis and results are presented in a normalized form; we define dimensionless parameters $h^*=h/H$, $L^*=L/H$, $S^*=S/H$ and $a^*=a/H$. As we are considering long beams with repeating structures loaded by a pure moment for which adhesion behavior varies periodically, it is unnecessary to define an absolute crack length and a here is defined as the crack front position relative to the front edge of the inset. a is normalized with respect to the beam height, H, as it is the only dimension that is not varied in the study and it is also convention to normalize the coordinate along the interface of a DCB with respect to the beam height (Maugis, 2000). $a^*=0$ is defined at the front edge of the inset and left to right is

defined as the positive direction since the crack is assumed to propagate from left to right as shown in Fig. 1(a).

2D plane strain is assumed in the model and it is solved under the conditions of small strain linear elasticity. Each component in the heterogeneous beam was assumed to be isotropic. The FE model was meshed with 4-node plane strain quadrilateral, reduced integration elements (CPE4RH). Mesh density was determined through a convergence study.

The effective adhesion strength of an adhesive structure is generally related to the maximum force (P_{max}) reached during delamination. This force would be a critical performance metric in applications such as adhesive-based-robotic grippers and stamps used in microtransfer printing processes. The delamination of a beam in a DCB like configuration is moment driven even when loaded with force, P, at the end (i.e. the moment at the crack tip that causes delamination is M=$P\times$ crack length). The critical delamination moment is constant for a homogeneous DCB and periodic for a heterogenous DCB with periodic patterns (Fig. 1). Here, to remove the effect of crack length (which can be varied by changing the beam length), a moment-loaded DCB is considered and the critical moment is taken as the measure of the effective adhesion strength of the DCB. This also has the benefit of eliminating the effect of the transverse shear stresses, which can impact the behavior of a DCB (Maugis, 2000).

The compliance method was used to calculate the strain energy release rate, G, from the FE simulations as (Anderson, 2017):

$$G = \frac{M^2}{b}\frac{dC}{da}, \tag{2}$$

where G is the strain energy release rate, M is the applied moment, b is the width of the beam, C is the rotational compliance of single beam and a is the crack front position. In FE analysis, dC/da was calculated numerically as $\Delta C/\Delta a$ from two FE simulations at different crack lengths. By applying the fracture criterion G=G_c, the critical moment for delamination is then determined.

The beam geometry that is considered in FE is sufficiently long (200–400 mm depending on the inset length L and spacing S) to avoid edge effects with a height $H = 10$ mm. Note, to prove the nondimensionalized results are independent of the absolute specimen dimension, Fig. A1 shows the maximum moment (M^*_{max}) and the ratio of maximum moment to square root of effective bending rigidity ($M^*_{max}/D^*_{eff}{}^{1/2}$) as a function of L^* with S^*=L^* and h^*=0.1 for different beam height $H = 1$, 10, 100 mm, and it is evident that the nondimensionalized results do not change with changing H. The compliant matrix has a Young's modulus E_c=2 MPa and Poisson's ratio ν_c=0.49 (representative of common elastomers), which has a plane strain Young's modulus, $E_c{}^*$=$E_c/(1–\nu_c{}^2)$=2.63 MPa and bending rigidity D_0=$bE_c{}^*H^3/12$=2.2×10^{-4} N-m^2. The bending rigidity in the inset section (calculation of the bending rigidity D by Eq. (E2)) is fixed at $D = 0.13$ N-m^2 (corresponding to the case where the stiff inset has a Young's modulus E_s=2 GPa and Poisson's ratio ν_s=0.3 and $h = 1$ mm). As h is varied, the bending rigidity in the inset region is fixed at $D = 0.13$ N-m^2 by adjusting the modulus of the inset (E_s) for each h. The bending rigidity D and critical moment M_c of the heterogenous DCB were nondimensionalized with respect to the corresponding bending rigidity D_0 and critical moment M_0 of a homogenous DCB made of same compliant material with same dimensions. M_0 for the homogenous DCB was calculated using Eq. (1).

The effective bending rigidity of the heterogeneous beam D_{eff} (containing both a compliant section and an inset section) is found by considering pure bending of one section of the beam shown as in Fig. 1(b). The section containing one period of the structure with height H, length (L+S) bends symmetrically when subject to bending moment M. Through FE analysis of this section, the effective bending rigidity is calculated as

$$D_{eff} = \frac{M(L+S)}{\theta}, \tag{3}$$

where θ is the angle between two inclined edges of the section loaded by moment M.

We define D^*=D/D_0, D^*_{eff}= D_{eff}/D_0 and M^*=M_c/M_0. Since G_c and b are the same for all cases, M^* is independent of the G_c and b according to Eqs. (1) and (2). Note that as the critical force in a force loaded condition is P_c=M_c/(crack length) for both homogeneous and heterogenous DCBs, M^* can be regarded as the nondimensionalized critical force of the heterogeneous DCB with respect to corresponding homogenous DCB with the same crack length. Another important reference case is the corresponding bilayer beam (i.e. S^*=0), which has a bending rigidity D^*=609.8 and critical moment M^*=24.7, as calculated by Eq. (E4).

Interface stress distributions of DCBs at different a^* are also investigated through FE. Plane strain quadrilateral elements (CPE4RH) were used and the mesh size near the crack tip was refined. Mesh size was determined by a convergence study and approximately 1×10^5 elements were used in each case. The distance along the interface from the crack front is denoted as x with positive direction defined as the crack propagation direction (i.e., left to right is defined as the positive direction in Fig. 1(a)) and is normalized as x^*=x/H. The normal stress along the adhered interface is denoted as σ_{zz} and is normalized as $\sigma^*_{zz} = \sigma_{zz}/(M/bH^2)$. The crack opening displacement is also extracted and is denoted as U_z and is normalized as $U^*_z = U_z/(M/(E_c{}^*bH))$.

2.2. Specimen fabrication for validation experiments

DCB specimens consisting of two identical beams with a polydimethylsiloxane (PDMS) matrix and a stiff rectangular inset of poly (methyl methacrylate) (PMMA) were fabricated via a molding process. Each beam of the DCB had a single rectangular inset. The beam geometries were as follows: overall length L_{all}=80.0 ± 0.4 mm, thickness $H = 12.5 \pm 0.2$ mm, width $b = 25.5 \pm 0.2$ mm, compliant layer thickness $h = 2.8 \pm 0.1$ mm, and inset lengths of $L = 10.0 \pm 0.1$ mm, 20.0 ± 0.1 mm, 30.0 ± 0.1 mm and 40.0 ± 0.1 mm. The front edge of the inset is always placed at 40.0 ± 0.2 mm from the front edge of the beam. In these specimens, the PDMS matrix has a Young's modulus E_c=2 MPa and Poisson's ratio ν_c=0.49 and the stiff PMMA inset has Young's modulus E_s=3 GPa and Poisson's ratio ν_s=0.37.

The molds were made from several PMMA sheets that were laser cut to the required geometry, stacked, and then assembled using

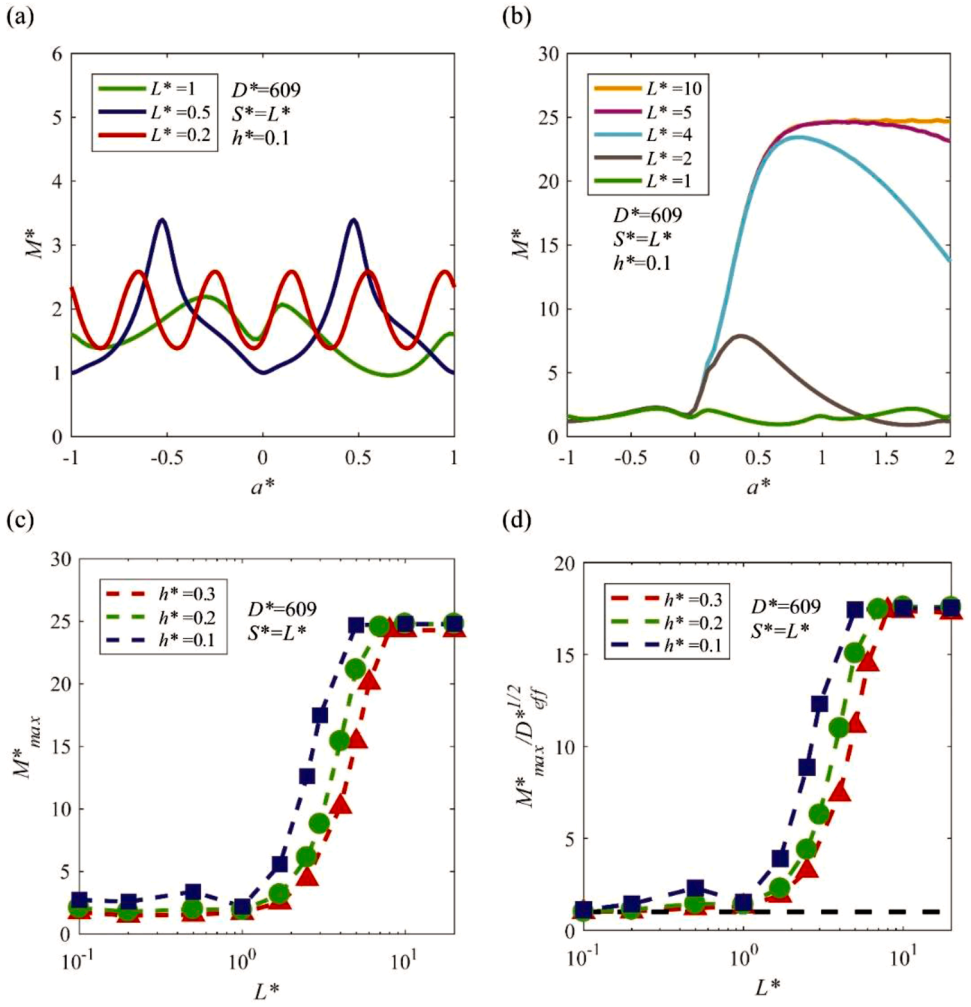

Fig. 2. Critical moment (M^*) for delamination of DCB specimen with $L^*=S^*$ (with constant bending rigidity $D^*=609$ in the inset region): (a) Critical moment (M^*) as a function of crack front position for $L^*\leq 1$ and $h^*=0.1$. (b) Critical moment as a function of crack front position for $L^*\geq 1$ and $h^*=0.1$. (c) Maximum moment (M^*_{max}) achieved during delamination for various L^* and h^*. (d) Ratio of maximum moment to square root of effective bending rigidity ($M^*_{max}/D^*_{eff}{}^{1/2}$) for various L^* and h^* ($M^*_{max}/D^*_{eff}{}^{1/2}=1$ based on Eq. (1) is shown as dashed black curve).

screws. Covers to the molds were also made from a PMMA sheet by laser cutting. The rectangular insets were made from transparent PMMA sheets by laser cutting. The molds and covers were treated with trichloro (1H, 1H, 2H, 2H-perfluorooctyl) silane (Sigma Aldrich, St. Louis, MO) for 4 h to facilitate release. The PMMA insets were treated with 1200 OS primer (Dow Corning, Midland, MI) to enhance adhesion to PDMS and then placed into the molds at the desired location. PDMS (Sylgard 184, Dow Corning Corporation, Midland, MI) with a 10:1 wt ratio of base elastomer to curing agent was prepared, degassed for 30 min in vacuum, poured into the molds. Covers were then applied on the top of the molds and clamped. The mold assemblies were heated in an oven at 85 °C for 4.5 h to cure the PDMS. After cooling, the beams were removed from the mold.

2.3. Experimental measurements of DCB adhesion

The DCB specimens consisting of two identical beams were tested in a standard universal testing machine (MTS Criterion Model 43) fitted with a 50 N load cell (MTS LSB.501). To mount the specimens in the machine, machined aluminum loading blocks with through holes were attached to both beams using a thin layer of silicone sealant (8661, 3 M, St. Paul, MN). The specimens were then mounted in clevises on the test machine with dowel pins (a photograph of a fabricated DCB specimen mounted on the experimental setup is shown in Fig. 8(a)). The specimens were loaded in displacement control at a rate of 5 mm/min and force and displacement data were recorded.

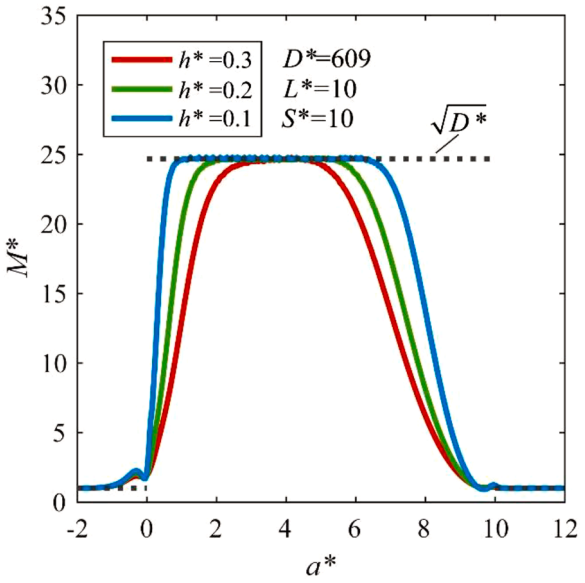

Fig. 3. Critical moment (M^*) for delamination as a function of crack front position for a DCB with L^*=10 and S^*=10. A prediction from a beam theory model is shown as dashed line and FE results are shown as solid lines.

3. Results and discussion

3.1. Numerical results

The effect of inset dimensions (L^*, S^* and h^*) on the critical moment for delamination is first examined for cases in which the inset length and spacing are the same (S^*=L^*). The critical moment as a function of crack front position for a range of L^* with h^*=0.1 is shown in Fig. 2(a) and (b) (the critical moments within one period of the inset pattern for various L^* with the crack front position normalized by inset length are shown in Fig. B1). The critical moment (Fig. 2(a)) fluctuates periodically due to the presence of the repeated inset pattern and the period of the moment fluctuation is equal to the period of the inset pattern, which is equal to L^*+S^*. As shown in Fig. 2(b), the maximum moment increases significantly as L^* increases for $L^*\geq$1 and the maximum moment plateaus to the corresponding bilayer DCB value for $L^*\geq$5. Fig. 2(c) summarizes the maximum moment (M^*_{max}) as a function of L^* and h^*, which is the moment required to delaminate the beam. The maximum moments depend strongly on the dimension of the inset pattern and three regions can be identified: (1) for $L^*\leq$1 there is a minimal change in M^*_{max} as L^* changes; (2) for $L^*>$1 and $L^*< L^*_{min}$ (L^*_{min}=~5 for h^*=0.1, L^*_{min}=~7 for h^*=0.2, L^*_{min}=~8 for h^*=0.3), M^*_{max} increases rapidly as a function of L^*, and a smaller h^* results in a larger M^*_{max} for a given L^*; (3) M^*_{max} plateaus for $L^*> L^*_{min}$ with M^*_{max} = 24.7, which is equal to the prediction obtained from an analytical model of a bilayer beam. L^*_{min} is the minimum inset length to realize M^*_{max}. Note that M^*_{max} is not a monotonic function of L^* for $L^*\leq$~1 keeping S^*=L^*. This is because the critical moment is not only affected by the inset length (L^*) but also the spacing (S^*). As will be discussed later in the paper, when $S^*\leq$1.5, there is interaction between adjacent insets and this may affect M^*_{max}.

It is desirable to have a beam with both high effective adhesion strength (quantified in terms of M^*_{max}) and low bending stiffness (quantified by D^*_{eff}), and we evaluate the trade-off between compliance and adhesion of the beam in terms of ratio of the maximum moment to square root of effective bending rigidity ($M^*_{max}/{D^*_{eff}}^{1/2}$). A higher $M^*_{max}/{D^*_{eff}}^{1/2}$ is more favorable, and $M^*_{max}/{D^*_{eff}}^{1/2}$ is equal to 1 for any beam specimen that meets the assumptions of classical beam theory (Eq. (1)). The effective bending rigidity of the beam (D^*_{eff}) as a function of L^* and h^* with S^*=L^* is shown in Fig. F1. D^*_{eff} approaches 2, which is the value predicted by the beam theory (Eq. (F4)), as L^* increases. $M^*_{max}/{D^*_{eff}}^{1/2}$ is calculated based on Figs. 2(c) and F1 and is summarized in Fig. 2(d). For the S^*=L^* cases studied, $M^*_{max}/{D^*_{eff}}^{1/2}$ is greater than one and the trends are similar to the trends observed for M^*_{max}. $M^*_{max}/{D^*_{eff}}^{1/2}$ increases rapidly for $L^*>$1 and plateaus for $L^*\geq L^*_{min}$, which corresponds to M^*_{max}=24.7 and D^*_{eff}=~2 when $L^*\geq L^*_{min}$. This suggests a segmented composite beam with L^*=S^* and $L^*>$0.1 always performs better than a homogeneous beam or a bilayer composite beam in terms of the trade-off between compliance and adhesion, and an inset design of $L^*\geq L^*_{min}$ leads to the highest adhesion per bending stiffness. In practice, specific application requirements (such as the spatial wavelength of the surface that the beam may need to conform to) may pose a limitation on the largest L^* that can be used, so L^* may not reach L^*_{min}. In such a scenario, it is desirable to avoid inset designs with $L^*<$1 and have an inset pattern with small h^* and the largest possible L^* for a given application.

Next, we release the constraint of L^*=S^* to examine a more general design space, and we start with the simplest case where the segmented composite beam contains insets with large L^* and S^* (i.e. L^*=10 and S^*=10). Fig. 3 shows the FE calculated critical moment for delamination as a function of crack front position as well as the critical moment from a beam theory-based analysis (calculated by Eq. (E4) and shown as a dotted line in Fig. 3). The FE results show a continuous change in the critical moment from the compliant homogenous region to the bilayer region over a finite length. Classical beam theory agrees with the FE predictions away from the

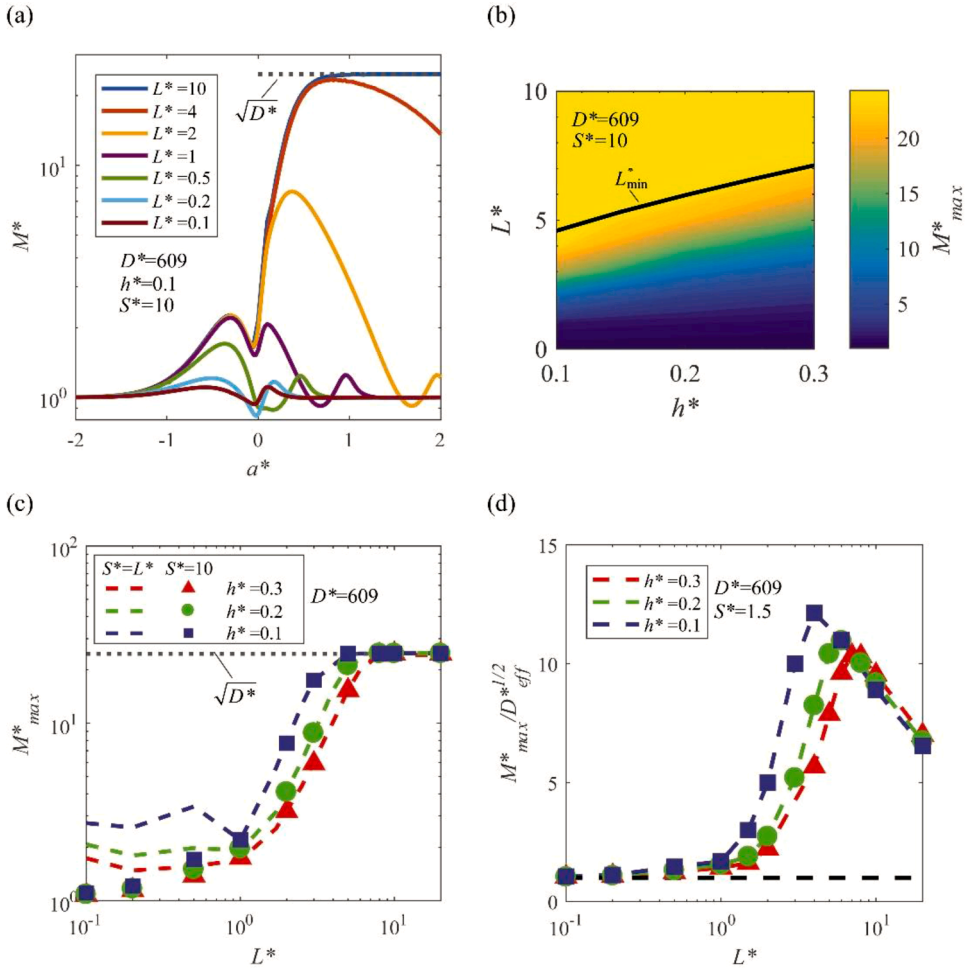

Fig. 4. Critical moment (M^*) for delamination of specimen with large S^* (with constant bending rigidity D^*=609 in the inset region): (a) Critical moment (M^*) for delamination as a function of crack front position for various L^* with S^*=10 and h^*=0.1. (b) Maximum moment (M^*_{max}) achieved during delamination for various L^* and h^* with S^*=10. (c) Comparison between maximum moment (M^*_{max}) achieved during delamination for L^*=S^* (denoted as dashed lines) and S^*=10 (denoted as symbols). (d) Ratio of maximum moment to square root of effective bending rigidity ($M^*_{max}/D^*_{eff}{}^{1/2}$) for various L^* and h^* with S^*=1.5 ($M^*_{max}/D^*_{eff}{}^{1/2}$=1 based on Eq. (1) is shown as dashed black curve).

transition region but is unable to predict the gradual change at the front edge (i.e., at a crack front position of a^*=0) and the back edge of the inset (a^*=10).

It has been widely acknowledged that the degree of confinement of a compliant layer will significantly alter the interface stress distribution and hence the effective adhesion strength (Benvidi and Bacca, 2021; Crosby et al., 2000; Luo et al., 2020; Luo and Turner, 2021). As the crack propagates into the inset containing region of the beam, the degree of confinement experienced by the crack tip first increases, then plateaus in a region away from the edges of the inset, and eventually decreases as it approaches the back of the inset. This leads to the gradual increase in the critical moment when a^*>0, the steady critical moment region, and the decrease near the back of the inset shown in Fig. 3. Fig. C1 shows the interface stress distribution and the crack opening displacement of a DCB with L^*=10, S^*=10 and h^*=0.1 when a^*=-5 (the crack front is within the compliant region of the DCB away from the inset, which is equivalent to the interface stress distribution and the crack opening displacement of a homogenous compliant DCB), a^*=0.3 (the crack front is within the inset containing region where the critical moment increases gradually), a^*=6 (the crack front is within the inset containing region where the critical moment reaches the steady value, which is equivalent to the interface stress distribution and the crack opening displacement of a long bilayer DCB) to illustrate the effect of confinement. As the confinement experienced by the crack tip increases (from a^*=-5 to a^*=0.3 to a^*=6), the crack opening displacement (Fig. C1(c)) and the magnitude of the stress concentration near the crack tip (Fig. C1(b)) both decrease.

The length where the critical moment increases gradually near the front of the inset (a^*=0 in Fig. 3) is denoted the front transition length, L^*_{front}, which is defined as the distance from front edge of the inset to the crack front position where the critical moment reaches 95% of the critical moment of the corresponding bilayer DCB. Through fitting of the FE results of beams containing insets with h^* varies from 0.1 to 0.7 and sufficiently large L^* and S^* as shown in Fig. D2(a) (FE results with h^* =0.1–0.3 are shown in

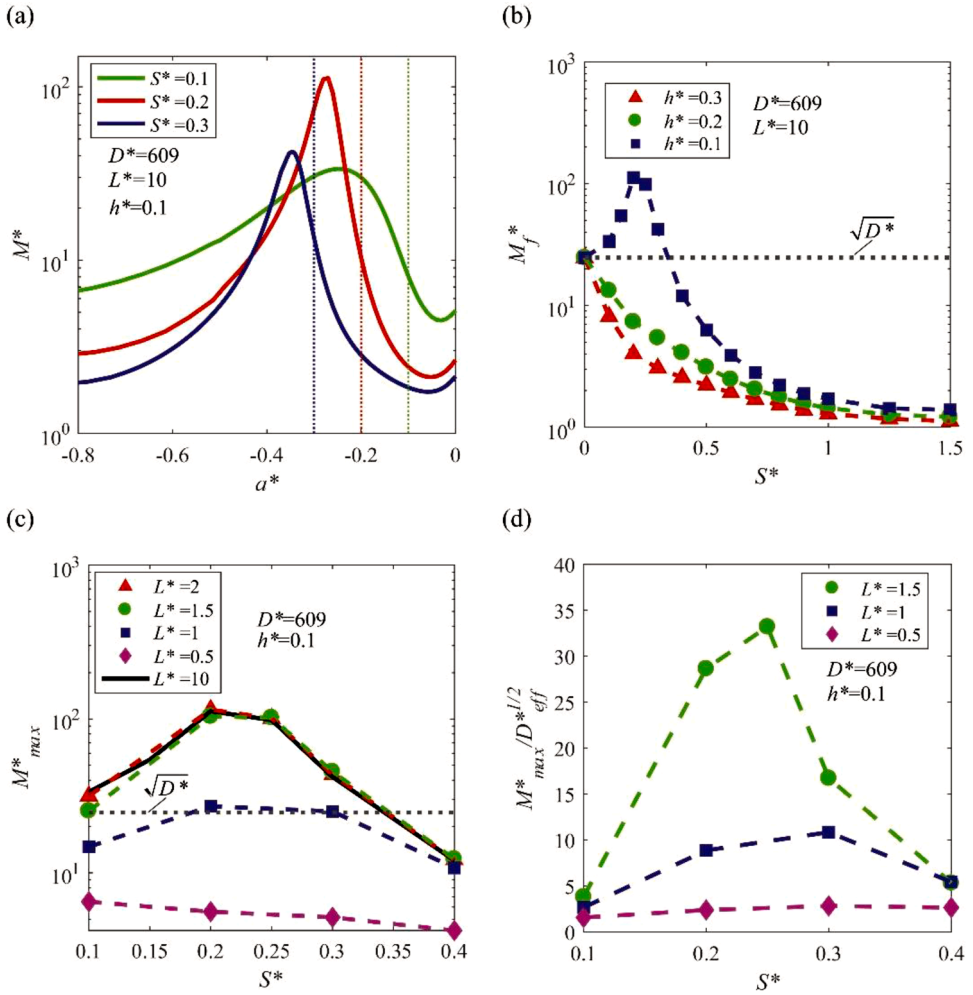

Fig. 5. Critical moment (M^*) for delamination of DCB specimen with small S^* (with constant bending rigidity D^*=609 in the inset region): (a) Critical moment (M^*) for delamination as a function of crack front position for various S^* with h^*=0.1, L^*=10 (dashed line indicates the position of the back edge of the inset). (b) Local maximum moment, M^*_f, achieved during delamination for various S^*, h^* and L^*=10. (c) Maximum moment, M^*_{max}, achieved during delamination for various L^*, S^* and h^*=0.1. (d) Ratio of maximum moment to square root of effective bending rigidity ($M^*_{max}/D^*_{eff}{}^{1/2}$) for various L^* and S^* with h^*=0.1.

Fig. 3 and FE results with h^*=0.4–0.7 are shown in Fig. D1(a)), the front transition length for a beam with D^*=609 is:

$$L^*_{front} \approx 7.2h^*. \tag{4}$$

D^* was varied in the simulations from 6.5 to 6088. From these simulations, we observed that the front transition length is only a function of h^* and is described by Eq. (4) when $D^* \geq \sim 10^2$. At $D^* < \sim 10^2$, L^*_{front} is a function of both h^* and D^*, and L^*_{front} is smaller for smaller D^* with a given h^*.

As noted above, a gradual decrease in critical moment is observed in the FE results as the crack approaches the back edge of the inset (a^*=10 in Fig. 3). This is due to reduced confinement near the crack tip as it approaches the back edge of the inset. The interface stress distribution and the crack opening displacement of a DCB with L^*=10, S^*=10 and h^*=0.1 when a^*=8 (the crack front is within the inset containing region where the critical moment decreases gradually) is also shown in Fig. C1. When the crack front is at a^*=8, the remaining inset section ahead of the crack front has lower effective stiffness compared to the case with the crack front at a^*=6 (the inset is sufficiently long ahead of the crack front), which leads to higher crack opening displacement and a stronger stress singularity at the crack tip. The deformation near the crack front of a DCB has often been described as "root rotation" that is captured by elastic foundation models (Kanninen, 1973; Li et al., 2004; Thouless, 2018; Williams, 1989) and such models can also provide insight into the behavior observed as the crack approaches the back edge of the inset. As the crack approaches the back edge, the remaining inset ahead of the crack front becomes shorter and the "root rotation" becomes more significant. An elastic foundation model to predict the critical moment near the back edge of the inset with a thin compliant layer underneath is presented in Appendix E, and there is reasonable agreement between this elastic foundation model and the FE results (Fig. E2).

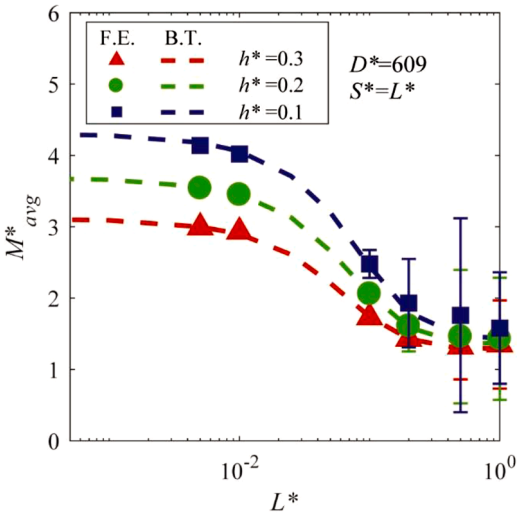

Fig. 6. Average moment, M^*_{avg}, for various L^*, S^* and h^* (with constant bending rigidity D^*=609 in the inset region). F.E. denotes the moment calculated from averaging the maximum moment and minimum moment in one period of the structure (M^*_{avg}=(M^*_{max}+M^*_{min})/2); the error bars represent ΔM^*= M^*_{max}−M^*_{min}; B.T denotes the moment calculated as $(D^*_{eff})^{1/2}$.

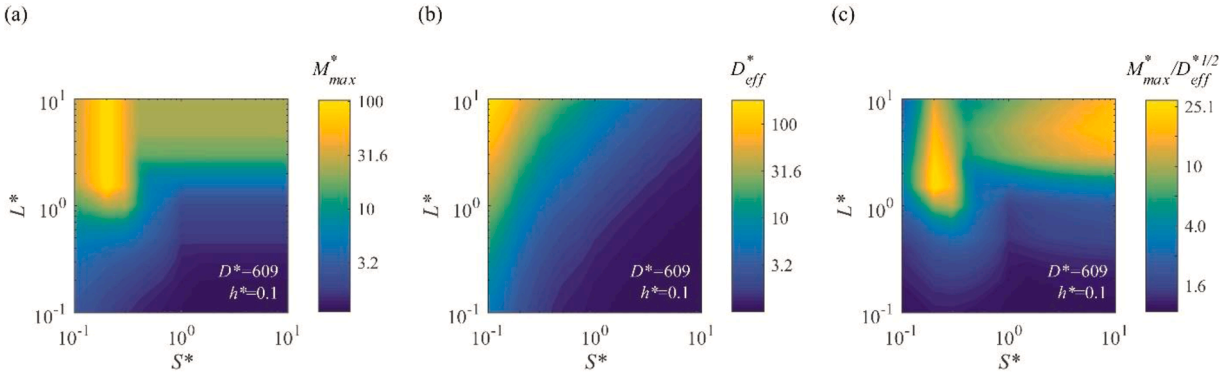

Fig. 7. (a) Maximum moment (M^*_{max}) achieved during delamination for various L^* and S^* with h^*=0.1. (b) Effective bending rigidity (D^*_{eff}) of the beam for various L^* and h^* with h^*=0.1. (c) Ratio of maximum moment to the square root of effective bending rigidity ($M^*_{max}/D^{*1/2}_{eff}$) for various L^* and S^* with h^*=0.1.

Similar to the front transition length, we define the back transition length, L^*_{back}, as the change in crack front position between where the moment is 95% of the critical moment of the bilayer DCB to the back edge of the inset. Through fitting the FE results in which h^* was varied from 0.1 to 0.7, as shown in Fig. D2(b), the L^*_{back} for a beam with D^*=609 is found to be

$$L^*_{back} \approx -4.3h^{*2} + 8.7h^* + 2.3. \tag{5}$$

While the front transition length (L^*_{front}), reaches a steady value for sufficiently large D^*, the back transition length (L^*_{back}), always increases as D^* increases. This is consistent with the results of elastic foundation model (Appendix E).

From Fig. 2(c), it is observed that the maximum critical moment that can be reached is the moment predicted by the bilayer beam theory solution (M^*=$(D^*)^{1/2}$). This critical moment is only reached if the inset is sufficiently long such that there is a region within the inset containing region where the crack front experiences the same confinement as the corresponding bilayer beam. Based on the front and back transition lengths described above, the minimum inset length to realize this maximum moment, L^*_{min}, can be calculated by

$$L^*_{\min} = L^*_{front} + L^*_{back}. \tag{6}$$

From Eqs. (4) and (5), it is apparent that $L^*_{\min}$ increases with increasing h^* even when D^* is constant. Thus, from a design standpoint, smaller h^* allows the maximum moment to be realized with shorter insets.

Effective bending rigidity of a beam (D^*_{eff}) with sufficiently large L^* and S^* can be calculated by Eq. (F4), which indicates lower D^*_{eff} can be achieved by reducing L^*/S^* while keep M^*_{max} unchanged with $L^* > L^*_{min}$. Though this case of long insets is helpful in understanding the mechanics, it has little potential for application as it requires a beam that has a subsurface inset pattern with a large period.

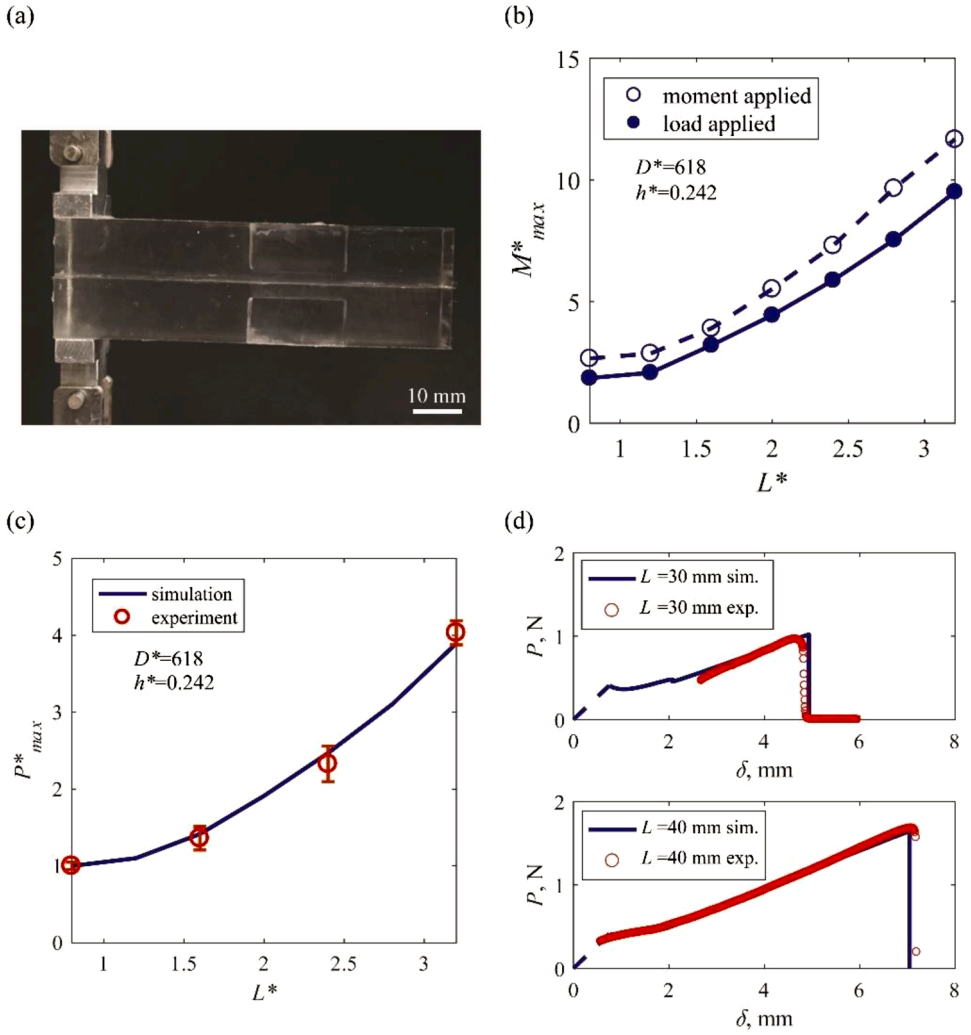

Fig. 8. (a) Photograph of a DCB mounted on the experimental setup. (b) Comparison between the maximum moment (M^*_{max}) for sufficient long DCB with moment applied and DCB with experimental dimension with force applied from FE simulations. (c) Comparison between the maximum force (P^*_{max}) for a single rectangular inset DCB with various L^* obtained from both experiments and FE simulations. (d) Comparison between experiment and FE results. Force-displacement curves for DCBs with single rectangular insets of L = 30 mm and L = 40 mm.

To validate the minimum inset length, $L^*_{\min}$ given by Eq. (6) and further understand the effect of inset length and spacing, we examine a series of cases in which S^* is sufficiently large to avoid interactions between the insets (S^*=10 in the FE simulation) and vary L^* and h^*. Fig. 4(a) shows the critical moment for delamination as a function of crack front position near the front edge of the inset (the critical moments within one period of the inset with the crack front position normalized by inset length are shown in Fig. B2) and, similar to results discussed earlier, the maximum M^* depends on L^*.

For insets with $L^* \geq L^*_{\min}$ (e.g., L^* =10 in Fig. 4(a)), the critical moment increases as the crack propagates into the inset containing region and reaches a steady critical moment in the region where the crack tip experiences the same confinement as a long bilayer beam. For insets with $L^* < L^*_{\min}$ (e.g., L^* =2 in Fig. 4(a)), the critical moment first increases for $a^*>0$ where the confinement increases and reaches a peak value smaller than $D^{*1/2}$, then the critical moment starts to decrease due to reduced confinement as the crack propagates towards the back edge of the inset. The interface stress distribution of the DCB with sufficiently large S^* and L^*=0.2, h^*=0.1 at a^*=0.35 (the crack front position where it reaches the peak critical moment) is also shown in Fig. C2. It is clear that the stress distribution at a^*=0.35 for L^*=2 is less confined compared to the corresponding bilayer beam, which leads to a higher stress concentration near the crack tip and lower critical moment compared with the bilayer beam. Fig. 4(b) shows the M^*_{max} as a function of h^* and L^*, when S^* is sufficiently large, M^*_{max} increases as L^* increases and plateaus to $M^*=(D^*)^{1/2}$ for $L^* \geq L^*_{\min}$, with $L^*_{\min}$ is given by Eq. (6).

The results in Fig. 4 can also be used to understand the potential for interactions between the insets. In Fig. 4(a), it is evident that M^* starts to increase from M^*=1 at an a^* of slightly less than -1. This increase in critical moment as the crack propagates from the compliant region towards the stiff region can be attributed to elastic toughening (Hossain et al., 2014; Hsueh et al., 2018; Kolednik

et al., 2011), where the stiff region ahead of the crack carries a higher stress compared to a homogenous compliant structure and reduces the stress concentration at the crack tip. This elastic toughening effect is evident in the stress distribution of a DCB with S^*=10, L^*=10 and h^*=0.1 at a^*=-0.35 (Fig. C3). A high tensile stress is observed near the front edge of the inset (a^*=-0.03, i.e., x^*=0.32 in Fig. C3(a)) – this reduces the crack opening displacement and the magnitude of stress singularity at the crack tip compared to the homogenous case. However, instead of increasing monotonically at $a^*<0$, M^* reaches a local maximum and then reduces to a local minimum right near the front edge of inset. Additional simulations have shown that such a non-monotonic trend at $a^*<0$ diminishes and finally vanishes as the compliant layer thickness (h^*) increases (Fig. D1(b)) or the Poisson's ratio of the compliant material (ν_c) decreases (Fig. D3(a)), which suggest that the decrease in critical moment at $a^*<0$ is related to the lateral confinement of the compliant material near the interface in front of the inset containing region. Note that in some cases with short insets (e.g., L^*=0.2 in Fig. 4(a)), M^* is smaller than 1. The stress distribution of a DCB with L^*=0.2 at a^*=0 is shown Fig. C4. As the short stiff inset rotates, a high compressive stress is generated near the back edge and the tensile stress near the front edge of the inset is elevated. This results in increased strain energy release rate at the crack tip and a M^* that is lower than that of the compliant homogeneous case.

The length ahead of the inset over which M^* deviates from the value of the compliant region (M^*=1) is denoted as the front spacing, S^*_{front}, and is defined as the distance between the crack front position at which the critical moment exceeds 5% of the critical moment for the compliant region and the front edge of the inset. Through fitting of the FE results of h^* varying from 0.1 to 0. 7, the front spacing for a beam with D^*=609 is:

$$S^*_{front} \approx -0.49h^{*2} - 0.06h^* + 1.3. \tag{7}$$

This result for S^*_{front} is independent of D^* for cases where $D^* \geq \sim 10$. As D^* decreases below ~10, S^* decreases with decreasing D^*.

As the crack approaches the back edge of the inset, fluctuation in the critical moment is observed (this occurs for all cases in Fig. 4 (a) but can only be seen for cases with $L^* \leq 1$). M^* reaches a local minimum around $a^*=L^*-0.3$ (i.e., the crack front position is 0.3 in front of the back edge of the inset), then increases to a local maximum around $a^*=L^*$, and returns to $M^*=1$ as the crack propagates into the compliant region away from the inset. Similarly, this fluctuation is caused by highly confined compliant layer with high Poisson's ratio, which diminishes as the compliant layer thickness increases (Fig. D1(c)) or the Poisson's ratio of the compliant material decreases (Fig. D3(b)). When $a^*=L^*$-0.3, compressive stress near the back edge of the inset and slightly elevated tensile stress near the crack tip is generated by the remaining short inset ahead of the crack tip (Fig. C5(a)). When $a^*=L^*$, The compliant thin layer with high Poisson's ratio near the back edge of the inset slightly confines the tensile strain near the crack tip compared to the homogenous compliant case and slightly reduces the magnitude of stress singularity at the crack tip (Fig. C5(b)).

The crack advance length beyond the back edge where the critical moment decreases to within 5% of M^*=1 is defined as the back spacing, S^*_{back}. Based on the FE results of h^* varying from 0.1 to 0.7 (Fig. D1(c)), the back spacing for a beam with D^*=609 was determined to be

$$S^*_{back} \approx 0.2 \tag{8}$$

for $h^*<0.4$ which is independent of D^* for $D^* \geq \sim 10$, and vanishes for $h^* \geq 0.4$.

For each inset to behave independently, S^*_{front} and S^*_{back} of two neighboring insets should not overlap, so the spacing between neighboring insets should be larger than a minimum spacing, $S^*_{\min}$:

$$S^*_{\min} = S^*_{front} + S^*_{back} \approx 1.5 \tag{9}$$

for the composite beam having a thin compliant layer underneath the inset.

Fig. 4(c) compares M^*_{max} for various L^* and h^* between $L^*=S^*$ (denoted as dashed lines) and S^*=10 (denoted as symbols). When $L^*<1$ (so $S^*<1$ for $L^*=S^*$), M^*_{max} achieved for $L^*=S^*$ and S^*=10 are different and M^*_{max} is always larger for $L^*=S^*$ due to interaction of neighboring insets. When $L^* \geq 1$, there is no difference in M^*_{max} between $L^*=S^*$ and S^*=10. The results shown confirm that if $S^* \geq S^*_{\min}$, S^* can be regarded as sufficiently large and each inset behaves independently, and this explains the second and third region observed in Fig. 4(c). It should be noted that even when $S^* < S^*_{\min}$, M^*_{max} may not be affected by the interaction of the insets. For example, for L^*=1 shown here, only the critical moment near back edge of the inset is different between the $S^*=L^*$ and S^*=10 cases (M^* at a^*=1 increases 29% for $S^*=L^*$ (Fig. 2(b)) compared with S^*=10 (Fig. 4(a)).), and M^*_{max} is almost the same.

In a microtransfer printing process (e.g., Meitl et al., 2006), it is desirable to control the adhesion within each period of the heterogeneous structure independently so that precise selective manipulation of individual chips can be achieved. This also holds for a soft robotic gripper, where independent control of local adhesion within each period of the structure enables more degrees of freedom in the operation and can simplify control (e.g. ability to controllably make contact with a low or high adhesion region depending on the manipulation task). The demand for independently controlled adhesion within each period of the structure requires sufficient spacing between insets ($S^* \geq 1.5$). When $S^* \geq 1.5$, M^*_{max} is determined by L^* and h^* as summarized in Fig. 4(b). The value of S^* when $S^* \geq 1.5$ only affects D^*_{eff} of the beam while it will not change M^*_{max}, which allows independent tuning of the compliance of beam and its adhesion. Effective bending rigidity of the beam (D^*_{eff}) as a function of L^* and h^* with S^*=1.5 is shown in Fig. F2. D^*_{eff} increases linearly as L^* increases and agrees well with the value predicted by the beam theory (Eq. (F4)), which suggests Eq. (F4) is capable to predict D^*_{eff} of a beam with $S^* \geq 1.5$. The corresponding $M^*_{max}/{D^*_{eff}}^{1/2}$ with S^*=1.5 is shown in Fig. 4(d). $M^*_{max}/{D^*_{eff}}^{1/2}$ increases rapidly for $L^*>1$ and achieves the peak value when $L^*=L^*_{min}$. Further increase of $L^*>L^*_{min}$ does not affect M^*_{max} but increases the D^*_{eff} of the beam as it increases L^*/S^*. In summary, a minimum spacing of S^*=1.5 is required to achieve independently controlled adhesion within each period of the structure, and an inset length $L^*=L^*_{min}$ is optimal to achieve high adhesion and favorable trade-off between

compliance and adhesion. Further increase of S^* beyond 1.5 if the application permits can lower D^*_{eff} while retaining the M^*_{max}.

Cases where $S^* \leq S^*_{\min}$ and neighboring insets interact were also investigated. We examined a series of cases where L^* is large (L^*=10 in the FE simulation) and S^* is small ($S^* \leq 0.5$). When L^* is sufficiently large and S^* is small, M^* is only affected by S^*. In this region between the two stiff insets, the crack front is influenced by both insets (we denote the inset ahead of this compliant region as the front inset and the inset behind this compliant region as the back inset). Fig. 5(a) shows M^* as a function of crack front position for various S^* with h^*=0.1. A local maximum is observed slightly in front of the back edge of the front inset (e.g., at around a^*=-0.27 for S^*=0.2, which means the crack front is around 0.07 in front of the back edge of the front inset. The positions of the back edge of the front inset for different S^* are denoted by the dashed lines in Fig. 5(a)) due to combination of elastic toughening of the back inset ahead of the crack and confinement of the compliant layer by the front inset near its back edge. The stress distribution for L^* sufficiently large, S^*=0.2 at a^*=-0.27 is shown in Fig. C6, and the pattern of the stress distribution is similar to the pattern for L^* and S^* sufficiently large at a^*=-0.35 (Fig. C3), but with the tensile stress near the crack tip further suppressed by the confinement of the front inset near its back edge. As the crack further propagates towards the front edge of the back inset, M^* drops as the effect of elastic toughening from the back inset is diminished and the confinement of the front inset decays. The stress distribution for L^* sufficiently large, S^*=0.2 at a^*=0 (Fig. C7) is thus observed to be similar to the stress distribution of L^* and S^* sufficiently large at a^*=0 (Fig. C3).

When S^* is reduced from 0.3 to 0.2, the local peak value increases because the coupled elastic toughening effect by the back inset and the confinement effect by the front inset is stronger with smaller S^*. However, when S^* is too small (S^*=0.1 here), the behavior begins to approach that of a bilayer beam and the peak becomes smaller and wider. As $S^* \to 0$ the moment will be constant and the peak will vanish. We define the value of the local maximum as M^*_f. Fig. 5(b) summarizes values of M^*_f for varying S^* and h^*. For h^*=0.1, M^*_f increases with decreasing S^* for $S^* > 0.2$ due to stronger elastic toughening and confinement effect and then decreases with decreasing S^* for $S^* < 0.2$ because of the homogenization effect noted above. For h^* of 0.2 and 0.3, M^*_f decreases with increasing S^* over the range investigated. This is because the stiff inset is further away from crack tip, reducing the effect of elastic toughening and confinement. Note that appropriate choice of h^* and S^* yields a M^*_f that is higher than the critical moment of bilayer DCB, which indicates higher maximum moment than the corresponding bilayer DCB. The above discussion of adhesion enhancement due to small S^* is limited to cases where L^* is large (L^*=10). In practical situations, one might want to achieve the adhesion enhancement above but with smaller L^*. Fig. 5(c) shows the M^*_{max} for various L^* and S^* with h^*=0.1. M^*_{max} increases as L^* increases and reaches the max M^*_f for long insets (Fig. 5(b)) when $L^* \geq 1.5$. This suggests L^* should be greater than or equal to 1.5 in order to maximize the peak value in moment obtained from small S^*.

$M^*_{max}/{D^*_{eff}}^{1/2}$ as a function of L^* and S^* with h^*=0.1 is shown in Fig. 5(d) and the corresponding D^*_{eff} is shown in Fig. F3. A maximum $M^*_{max}/{D^*_{eff}}^{1/2}$ of 33 is achieved with L^*=1.5, S^*=0.25 and h^*=0.1, and the corresponding D^*_{eff} is 9.5.

Lastly, we examine the case where both L^* and S^* are small. Fig. 6 shows the average moment, M^*_{avg}, and the difference in maximum moment and minimum moment (ΔM^*) for small L^* ($L^* \leq 1$) with $S^*=L^*$. When the period of the inset structure (L^*+S^*) is small enough, ΔM^* becomes negligible and M^* is nearly constant. This is not unexpected because in many composites, the system is treated as a homogenous material when the components are below a critical length scale. Beyond results obtained from FE that simulate the delamination of the heterogeneous DCB directly (denoted as F.E. in Fig. 6), results predicted by beam theory with the average moment (M^*_{avg}) calculated as ${D^*_{eff}}^{1/2}$ are also shown as comparison (denoted as B.T. in Fig. 6). It is clear that the $M^*_{\max}$ from the FE and homogenized analysis agree with each other reasonably well when $(L^*+S^*) < 0.2$ for all h^* studied, which provides a cut-off for using a homogenized analysis and suggests that $(L^*+S^*) < 0.2$ is not a favorable design space as it is still limited by the scaling relation in Eq. (1). Moreover, M^*_{avg} increases as L^* is reduced and plateaus. The plateau value is larger for smaller h^* even D^* is kept constant. This is because the deformation is mainly taken by the compliant matrix. For small L^* and h^* investigated here, smaller L^* and h^* indicate more confinement for the soft matrix, which increases the effectively bending rigidity of the beam and the critical bending moment.

Beam-type structures that have specific adhesion responses and bending compliance have applications in microtransfer printing and robotic gripping. Recent development in commercial multi-material 3D printing has enabled controllable and reliable fabrication of structures with structured heterogeneity and motivates the use of controlled elastic heterogeneity in a beam type structure to achieve targeted adhesion and compliance. The design space for such structures is summarized in Fig. 7 through the maximum moment (M^*_{max}), effective bending rigidity (D^*_{eff}), and $M^*_{max}/{D^*_{eff}}^{1/2}$ as a function of L^* and S^* from 0.1 to 10 with h^*=0.1. From Fig. 7, it is evident that high $M^*_{max}/{D^*_{eff}}^{1/2}$ is achieved when both L^* and S^* are large, or when L^*=1.5 and S^*=0.25.

3.2. Experimental validation

As discussed earlier, applications such as microtansfer printing and robotic gripping could benefit from a beam where there are distinct regions with different adhesion. Thus, in the experiments, the case with large enough spacing (S^*) was examined. When the spacing is sufficiently large, the compliance of the beam can be tuned by changing S^* while the adhesion of the beam is determined by L^*. Specifically, we conducted experiments on DCBs containing a single rectangular inset to demonstrate the effect of L^* on adhesion when S^* is sufficiently large and compared with FE results. Single rectangular inset DCBs with an overall length L_{all}=80.0 ± 0.4 mm, thickness $H = 12.5 \pm 0.2$ mm and width $b = 25.5 \pm 0.2$ mm with a compliant layer thickness $h = 2.8 \pm 0.1$ mm and insets of varying lengths: $L = 10.0 \pm 0.1$ mm, 20.0 ± 0.1 mm, 30.0 ± 0.1 mm or 40.0 ± 0.1 mm (which gives L^*=0.8, 1.6, 2.4 and 3.2), were tested. The stiff insets of the DCB specimens were made of PMMA. PDMS is chosen as the compliant matrix since it is a commonly used elastomer in microtansfer printing and soft robotics and its adhesion is widely investigated under framework of linear elastic fracture mechanics (Carlson et al., 2011; Khaderi et al., 2015; Kim et al., 2012; Minsky and Turner, 2017, 2015). A photograph of a DCB specimen mounted in the experimental setup is shown in Fig. 8(a).

Different from the configuration shown in Fig. 1 where moments are applied to the DCB, the experiments are conducted under displacement control in which transverse loads are applied to the end of the DCB specimens. The applied loads create moments as well as shear forces at the crack tip. Fig. 8(b) compares the maximum moment (M^*_{max}) obtained from FE between DCBs with moments applied and DCBs with the experimental dimensions described above with transverse loads applied. An equivalent maximum moment (M^*_{max}) for the force-loaded configuration is $M^*_{max}=(P_{max}\times a_c)/M_0$, where P_{max} is the maximum force achieved and a_c is the corresponding critical crack length. While M^*_{max} is always higher for a DCB loaded by pure moments, the overall trend and the relative change in critical moment as a function of L^* between the two configurations are very similar. M^*_{max} increases 5.1 and 4.5 times when L^* increases from 0.8 to 3.2 for the moment case and force case, respectively. This suggests that the experimental configurations tested are moment dominated and can reasonably be compared to the modeling results in this paper where moments are applied. Since the front edge of the inset is always placed at the same location in the DCB specimen, the critical crack length a_c changes only slightly compared to the change of M^*_{max}, and the change of M^*_{max} is mostly a result of a change in P_{max}. As a result, P_{max} obtained in displacement-controlled experiments is appropriate to validate the FE results.

Fig. 8(c) shows the maximum force (P^*_{max}) measured in the experiments along with the FE results. The maximum force is presented in a dimensionless form and is nondimensionalized with respect to the maximum force obtained when $L^*=0.8$ (which is 0.42 N for the $L = 10$ mm case). The maximum force increases 4.0 times (from 0.42 N to 1.68 N) when L^* increases from 0.8 to 3.2 (inset length increases from 10 mm to 40 mm), and good agreement between experiments and simulations over the range of inset lengths tested is observed. Fig. 8(d) shows typical experimental force-displacement curves. It should be noted that the compliant matrix of the DCB is made of PDMS and thus the crack will heal itself if the crack faces are allowed to contact, thus we prescribe a small displacement on the DCB specimen at the beginning of the test in order to maintain an initial crack – this is the reason the experimental data in Fig. 8 (d) begins at a finite displacement. Force-displacement curves predicted from the FE model are also shown in Fig. 8(d) and agree reasonably well with the experiments. The toughness, G_C, used in the FE curves in Fig. 8(d) was determined by finding the toughness that allowed for the best fit across all of the experiments and was determined to be $G_c=0.46 \pm 0.07$ J/m^2.

4. Summary

The adhesion behavior of beams with segmented subsurface elastic heterogeneity were investigated. It is found that when the spacing between insets is larger than 1.5 times height of the beam ($S^*\geq 1.5$), each inset behaves independently and the value of the spacing only affects the effective bending rigidity of the beam. The maximum moment achieved during delamination increases as the inset length increases and plateaus to a value of the corresponding bilayer beams if the inset is larger than a critical inset length ($L^*\geq L^*_{min}$) which depends on compliant layer thickness underneath the inset and elastic mismatch. If the spacing between insets is smaller than 1.5 times height of the beam ($S^*<1.5$), there is interaction between insets which might increases the maximum moment compared to the case where each inset behaves independently. The segmented composite beams investigated generally have a higher maximum moment compared to a homogeneous or a layered composite beam that has the same effective bending rigidity, except for the case where both spacing and inset length are small (i.e. $(L^*+S^*)\leq 0.2$), in which case the beam behaves like a homogenous beam with an effective composite modulus. Finally, the modeling results were validated via experiments on DCBs containing single inset. In summary, this work provides an understanding of how subsurface elastic heterogeneity can be used to control the delamination behavior of beams and it gives guidance for the design of heterogeneous beams containing insets to realize controlled adhesion for applications such as soft robotic grippers and microtransfer printing.

CRediT authorship contribution statement

Aoyi Luo: Conceptualization, Formal analysis, Investigation, Validation, Writing – original draft, Writing – review & editing. **Kevin T. Turner:** Conceptualization, Supervision, Writing – review & editing.

Declaration of Competing Interest

The authors declare that they have no known competing financial interests or personal relationships that could have appeared to influence the work reported in this paper.

Acknowledgments

This work was supported by the National Science Foundation under award 1663037 and 1761726. The authors thank Professor John L. Bassani and Gnana Saurya Vankayalapati for providing helpful comments on the manuscript.

Appendix A

Effect of the absolute beam dimension

Effect of the absolute dimension of the beam is investigated by studying the maximum moment (M^*_{max}) and the ratio of maximum moment to square root of effective bending rigidity ($M^*_{max}/D^*_{eff}{}^{1/2}$) as a function of L^* with $S^*=L^*$ and $h^*=0.1$ for different beam height $H = 1$, 10, 100 mm. The simulation results summarized in Fig. A1 show that the nondimensionalized results are independent of the absolute specimen dimension.

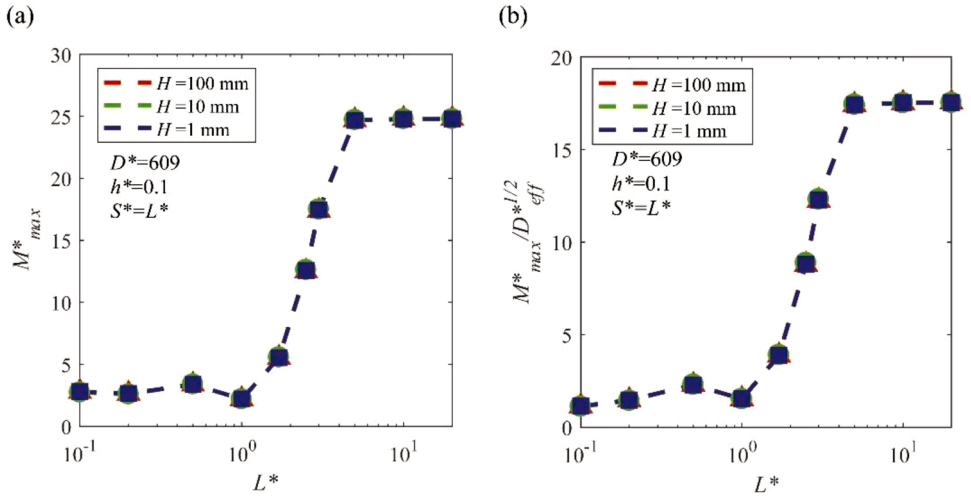

Fig. A1. (a) Maximum moment (M^*_{max}) achieved during delamination as a function of L^* with $S^*=L^*$ and $h^*=0.1$ for different beam height H. (b) Ratio of maximum moment to square root of effective bending rigidity ($M^*_{max}/D^{*1/2}_{eff}$) as a function of L^* with $S^*=L^*$ and $h^*=0.1$ for different beam height H.

Appendix B

Critical moment as a function of crack front position within one period.

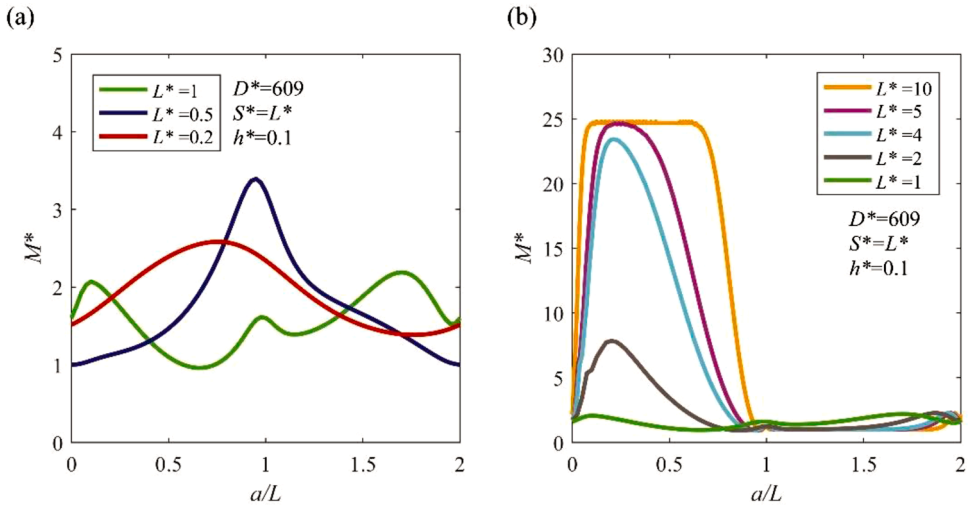

Fig. B1. (a) Critical moment (M^*) as a function of crack front position for $L^*\leq 1$, $L^*=S^*$ and $h^*=0.1$ with the crack front position normalized by inset length. (b) Critical moment as a function of crack front position for $L^*\geq 1$, $L^*=S^*$ and $h^*=0.1$ with the crack front position normalized by inset length.

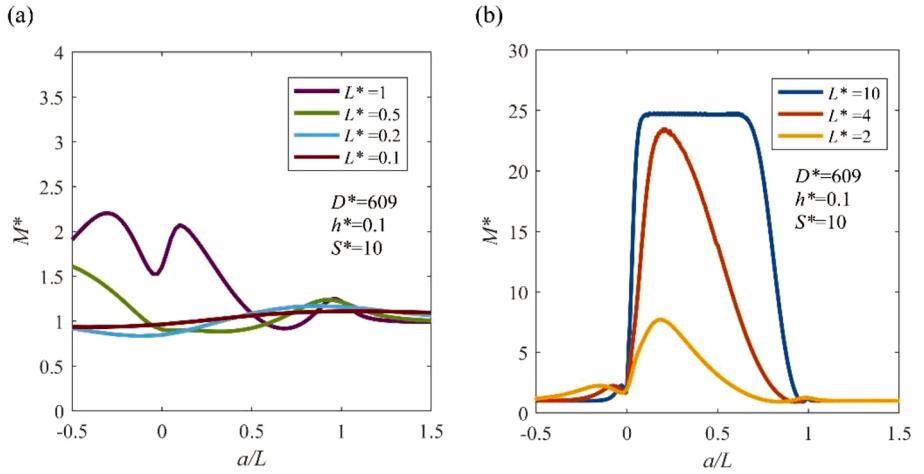

Fig. B2. (a) Critical moment (M^*) as a function of crack front position for $L^*\leq 1$, $S^*=10$ and $h^*=0.1$ with the crack front position normalized by inset length. (b) Critical moment as a function of crack front position for $L^*\geq 1$, $S^*=10$ and $h^*=0.1$ with the crack front position normalized by inset length.

Appendix C

Interface stress distribution of the DCB.

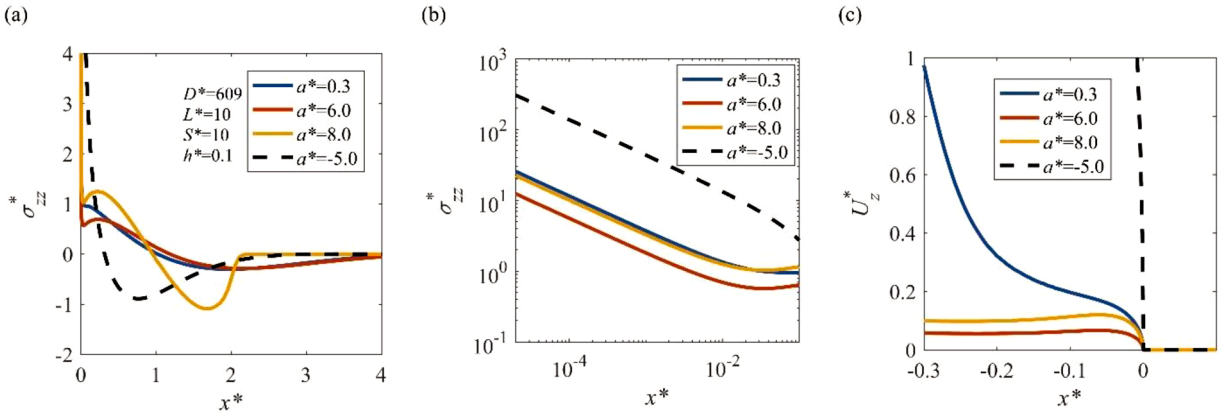

Fig. C1. (a) Interface normal stress distributions as a function of the distance from the crack front (x^*) at different crack front positions for $S^*=L^*=10$ and $h^*=0.1$. (b) Interface normal stress distributions near the crack front as a function of the distance from the crack front (x^*) at different crack front positions for $S^*=L^*=10$ and $h^*=0.1$. (c) Crack opening displacement as a function of the distance from the crack front (x^*) at different crack front positions for $S^*=L^*=10$ and $h^*=0.1$.

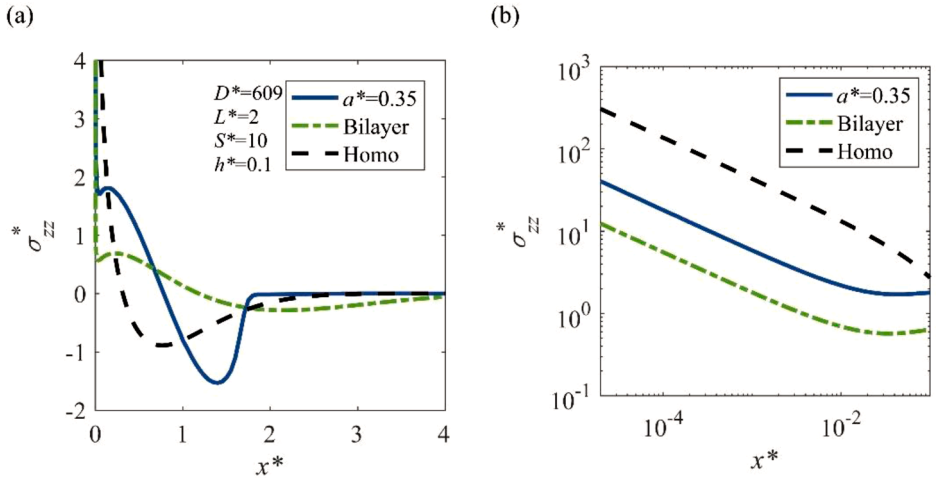

Fig. C2. (a) Interface normal stress distributions as a function of the distance from the crack front (x^*) at crack front a^*=0.35 for S^*=10, L^*=2 and h^*=0.1. (b) Interface normal stress distributions near the crack front as a function of the distance from the crack front (x^*) at crack front a^*=0.35 for S^*=10, L^*=2 and h^*=0.1.

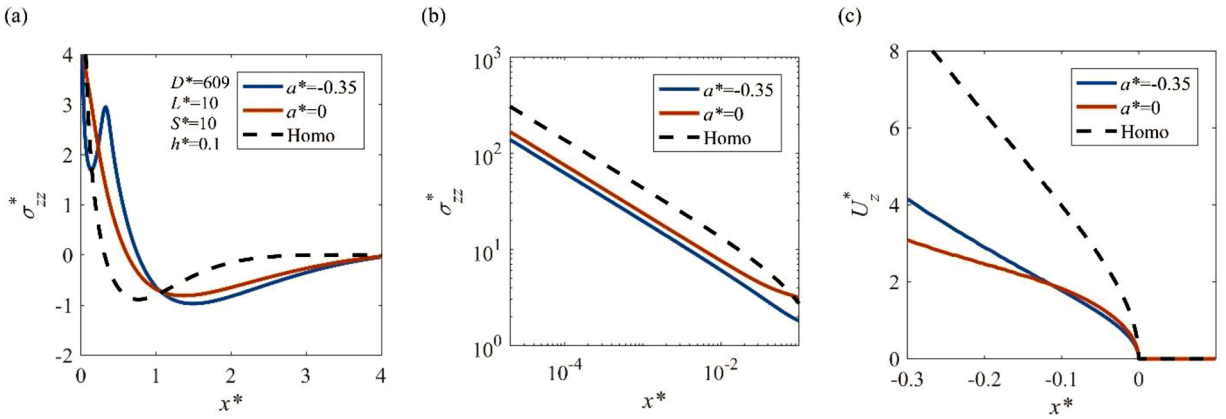

Fig. C3. (a) Interface normal stress distributions as a function of the distance from the crack front (x^*) at crack front positions a^*=-0.35 and a^*=0 for S^*=L^*=10 and h^*=0.1 (The interface stress distribution of a homogenous DCB is shown as a dashed line). (b) Interface normal stress distributions near the crack front as a function of the distance from the crack front (x^*) at crack front positions a^*=-0.35 and a^*=0 for S^*=L^*=10 and h^*=0.1 (The interface stress distribution of a homogenous DCB is shown as a dashed line). (c) Crack opening displacement as a function of the distance from the crack front (x^*) at crack front positions a^*=-0.35 and a^*=0 for S^*=L^*=10 and h^*=0.1 (The crack opening displacement of a homogenous DCB is shown as a dashed line).

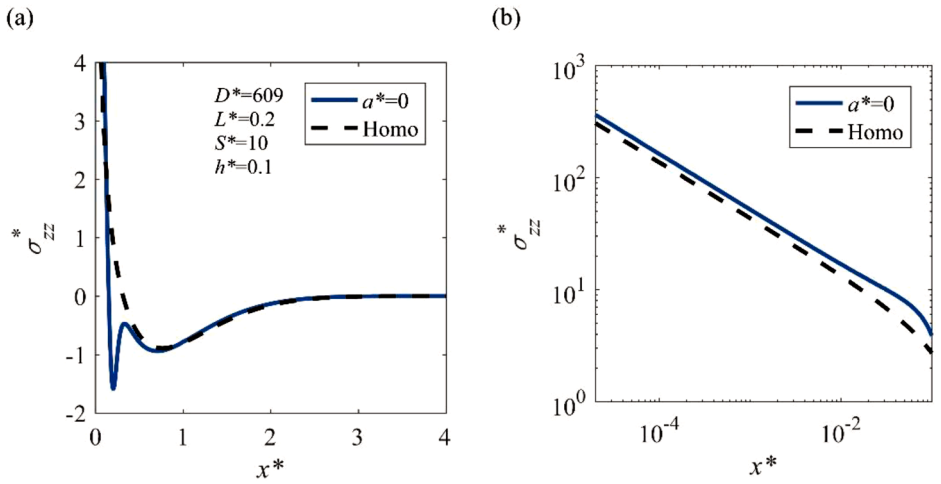

Fig. C4. (a) Interface normal stress distributions as a function of the distance from the crack front (x^*) at crack front position a^*=0 for S^*=10, L^*=0.2, h^*=0.1 (The interface stress distribution of a homogenous DCB is shown as a dashed line). (b) Interface normal stress distributions near the crack front as a function of the distance from the crack front (x^*) at crack front position a^*=0 for S^*=10, L^*=0.2, h^*=0.1 (The interface stress distribution of a homogenous DCB is shown as a dashed line).

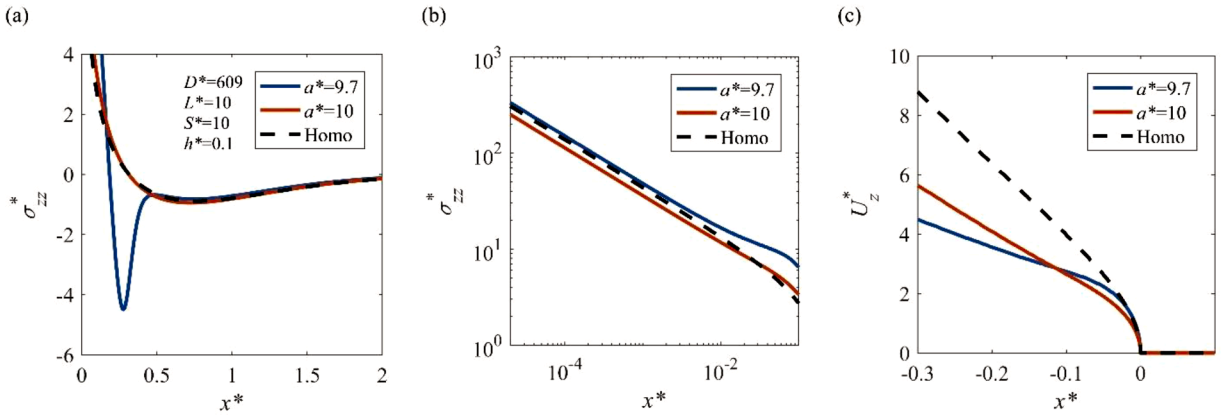

Fig. C5. (a) Interface normal stress distributions as a function of the distance from the crack front (x^*) at crack front position a^*=9.7 and 10 for S^*=10, L^*=10, h^*=0.1 (The interface stress distribution of a homogenous DCB is shown as a dashed line). (b) Interface normal stress distributions near the crack front as a function of the distance from the crack front (x^*) at crack front position a^*=9.7 and 10 for S^*=10, L^*=10, h^*=0.1 (The interface stress distribution of a homogenous DCB is shown as a dashed line). (c) Crack opening displacement as a function of the distance from the crack front (x^*) at crack front position a^*=9.7 and 10 for S^*=10, L^*=10, h^*=0.1 (The crack opening displacement of a homogenous DCB is shown as a dashed line).

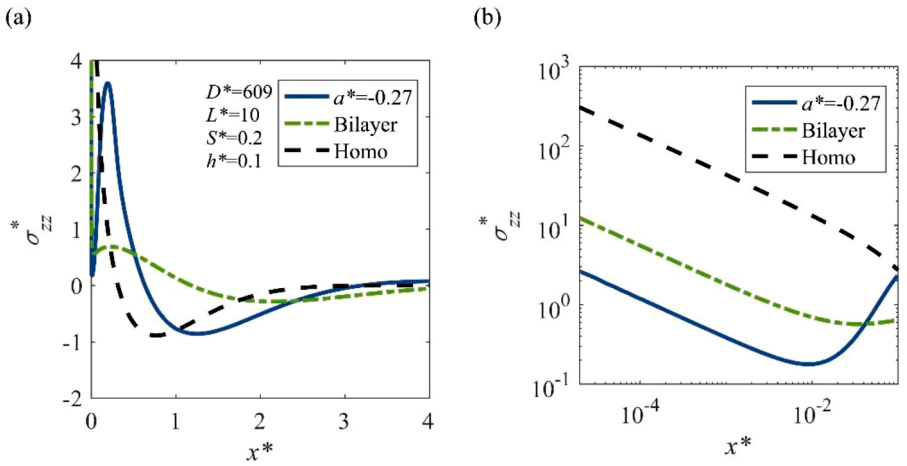

Fig. C6. (a) Interface normal stress distributions as a function of the distance from the crack front (x^*) at crack front position a^*=-0.27 for S^*=0.2, L^*=10, h^*=0.1. (b) Interface normal stress distributions near the crack front as a function of the distance from the crack front (x^*) at crack front position a^*=-0.27 and 10 for S^*=0.2, L^*=10, h^*=0.1.

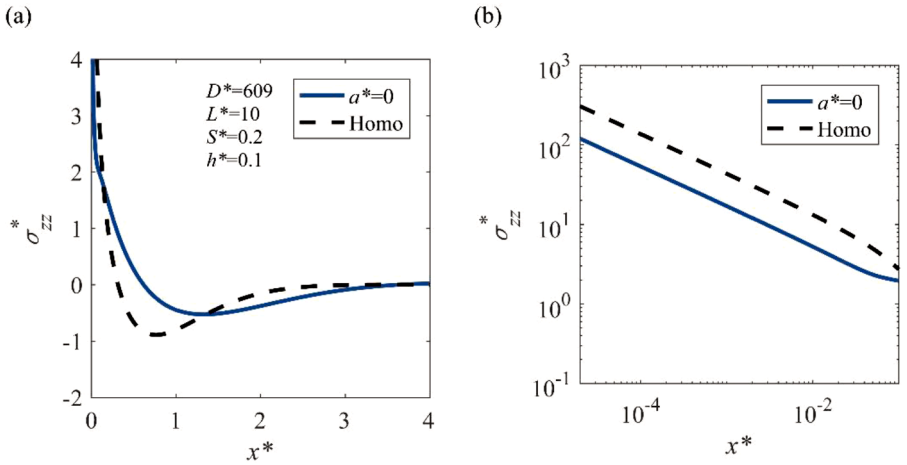

Fig. C7. (a) Interface normal stress distributions as a function of the distance from the crack front (x^*) at crack front position a^*=0 for S^*=0.2, L^*=10, h^*=0.1 (The interface stress distribution of a homogenous DCB is shown as a dashed line). (b) Interface normal stress distributions near the crack front as a function of the distance from the crack front (x^*) at crack front position a^*=0 for S^*=0.2, L^*=10, h^*=0.1 (The interface stress distribution of a homogenous DCB is shown as a dashed line).

Appendix D

Critical transition length and spacing.

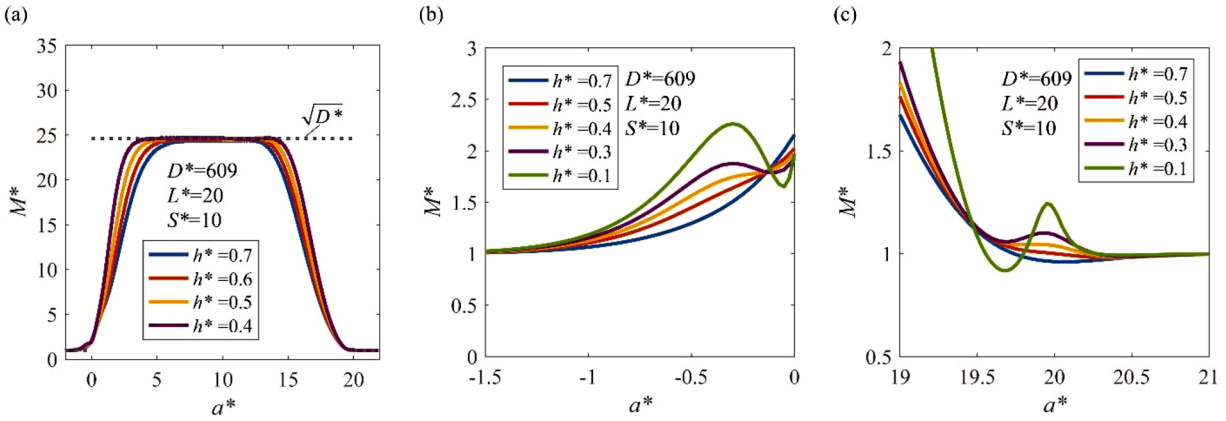

Fig. D1. (a) Critical moment (M^*) for delamination as a function of crack front position for a DCB with L^*=20, S^*=10 and various h^*. A prediction from a beam theory model is shown as dashed line and FE results are shown as solid lines. (b) Critical moment (M^*) for delamination as a function of crack front position near the front edge of the inset for a DCB with L^*=20, S^*=10 and various h^*. (c) Critical moment (M^*) for delamination as a function of crack front position near the back edge of the inset for a DCB with L^*=20, S^*=10 and various h^*.

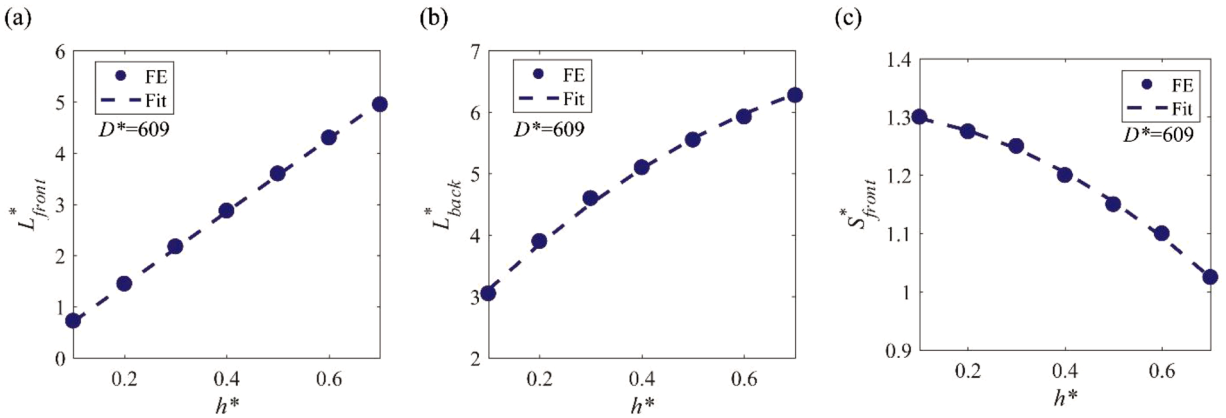

Fig. D2. (a) Front transition length (L^*_{front}) as a function of h^* (L^*_{front} calculated by the fitted Eq. (4) is denoted as "Fit" and shown as a dashed line). (b) Back transition length (L^*_{back}) as a function of h^* (L^*_{back} calculated by the fitted Eq. (5) is denoted as "Fit" and shown as a dashed line). (c) Front spacing (S^*_{front}) as a function of h^* (S^*_{front} calculated by the fitted Eq. (7) is denoted as "Fit" and shown as a dashed line).

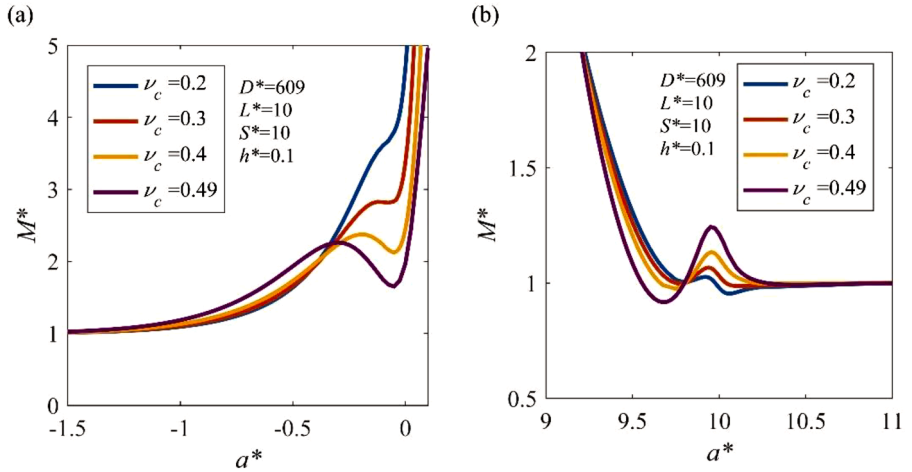

Fig. D3. (a) Critical moment (M^*) for delamination as a function of crack front position near the front edge of the inset for a DCB with L^*=10, S^*=10, h^*=0.1 and various ν_c. (b) Critical moment (M^*) for delamination as a function of crack front position near the back edge of the inset for a DCB with L^*=10, S^*=10, h^*=0.1 and various ν_c.

Appendix E

Compliance-based fracture analysis of double cantilever beam using classical beam theory.
Based on classical beam theory, *dC/da* for a moment-loaded beam is:

$$\frac{dC_{beam}}{da}(a) = \frac{1}{D(a)}, \tag{E1}$$

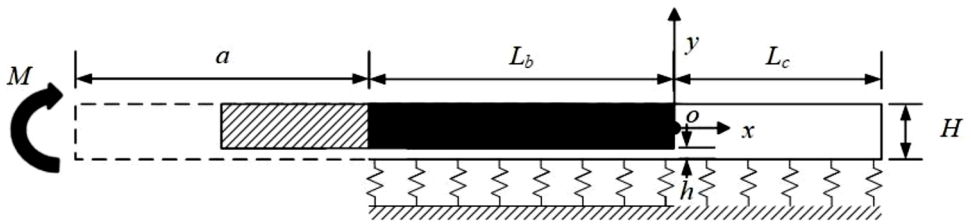

Fig. E1. Schematic of a composite beam supported on an elastic foundation.

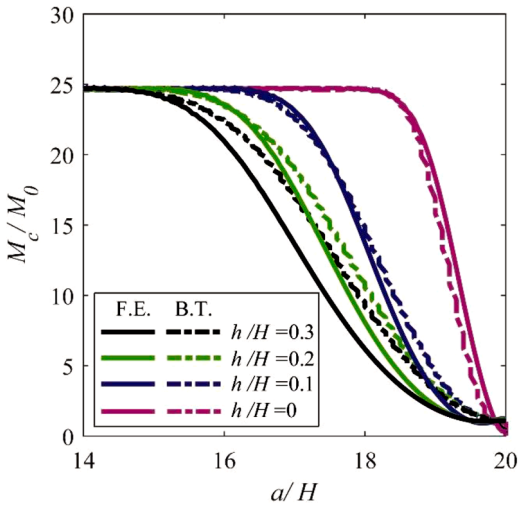

Fig. E2. Comparison of critical moment versus crack front position for DCB containing a single long rectangular inset; results obtained from finite element (F.E.) and elastic foundation beam theory (B.T.) model.

where C_{beam} is the rotational compliance of single beam derived via beam theory and $D(a)$ is the bending rigidity of the beam calculated at the crack tip cross section. For a homogenous beam section, $D = bE_c{}^*H^3/12$. For a bilayer beam section, D is calculated as (Gere and Goodno, 2009):

$$D = \frac{E_c^*}{3}\left[m^3 - (m-h)^3\right] + \frac{E_s^*}{3}\left[(m-h)^3 + (H-m)^3\right], \tag{E2}$$

where m is the distance from the neutral axis to the bottom edge of the beam calculated as:

$$m = \frac{h^2\left(E_c^* - E_s^*\right) + H^2E_s^*}{2h\left(E_c^* - E_s^*\right) + 2HE_s^*}. \tag{E3}$$

Based on Eqs. (2), (E1) and the Griffith fracture criterion, the critical moment for delamination is:

$$M_c = \sqrt{G_c \cdot b \cdot D(a)}. \tag{E4}$$

As is evident from Eq. (E4), the critical moment for a given crack front position only depends on the properties of the cross section at crack tip.

Compliance analysis using beam theory with root rotation

Eq. (E1) gives dC/dA obtained via classical beam theory. In addition to the bending of the loading arm of the beam, there is deformation ahead of the crack front. In order to account for the deformation ahead of the crack tip quantitatively, root rotation compliance θ_0, which is the rotation of the cross section at crack tip under unit moment applied, can be added to the compliance:

$$C(a) = C_{beam}(a) + \theta_0(a), \tag{E5}$$

where $C_{beam}(a)$ is the rotational compliance predicted by classical beam theory. Thus

$$\frac{dC}{da}(a) = \frac{dC_{beam}}{da}(a) + \frac{d\theta_0}{da}(a), \tag{E6}$$

where the first term on the right is calculated by Eq. (E1). This leads to a critical moment for delamination:

$$M_c = \sqrt{G_c \Big/ \left(\frac{dC_{beam}}{da}(a) + \frac{d\theta_0}{da}(a)\right)}. \tag{E7}$$

The elastic-foundation model developed by Kanninen (1973) has been widely used to account for the effect of root rotation (Li et al., 2004; Thouless, 2018; Williams, 1989). In this model, the presence of the other beam is modeled as a spring foundation with stiffness k bonded to a rigid surface and we further extended the analysis to composite beam considered in the present work (Fig. E1). To find the root rotation at the crack tip, the deformation of the beam ahead of the crack tip, as shown in Fig. E1, is considered. The coordinate system is located as shown so that $x = 0$ is at the back edge of the inset. Thus, the crack tip is at $x = -L_b$. L_b is the remaining length of the inset ahead of the crack tip. L_c is the remaining length of the beam behind inset. The beam ahead of the crack tip shown in Fig. E1 consists of two segments: a heterogenous segment ($-L_b \le x \le 0$) denoted segment 1 and a homogenous segment ($0 \le x \le L_c$) denoted segment 2. L_c is assumed to be sufficiently long such that there is no end effect from the end of the beam when crack is propagating in $x \le 0$.

Following the analysis of Kanninen (1973), the deflection of each segment is governed by

$$\frac{d^4y}{dx^4} + 4\lambda_i^4 y = 0, \tag{E8}$$

where $\lambda_i{}^4 = k_i/(4D_i)$ and $i = 1, 2$. k_i is the foundation stiffness of segment i. D_i is the bending rigidity of segment i. The boundary conditions at $x = -L_b$, a unit moment with no shear force is applied to satisfy equilibrium of beam section $x < -L_b$:

$$D_1 y''(-L_b) = 1, \tag{E9}$$

$$y'''(-L_b) = 0, \tag{E10}$$

and at $x = 0$, there is continuity in deflection, angle of rotation, moment, and force

$$y(0^-) = y(0^+), \tag{E11}$$

$$y'(0^-) = y'(0^+), \tag{E12}$$

$$D_1 y''(0^-) = D_2 y''; (0^+), \tag{E13}$$

$$D_1 y''(0^-) = D_2 y''(0^+), \tag{E14}$$

and at x=L_c, since L_c is sufficient long, there is no deformation:

$$y(L_c) = 0, \tag{E15}$$

$$y'(L_c) = 0. \tag{E16}$$

The general solution to Eq. (E8) is

$$y = e^{-\lambda_i x}(a_i \sin\lambda_i x + b_i \cos\lambda_i x) + e^{\lambda_i x}(c_i \sin\lambda_i x + d_i \cos\lambda_i x). \tag{E17}$$

Considering that the second segment, $i = 2$ ($0 \le x \le L_c$), is sufficiently long, to satisfy Eqs. (E15) and (E16), the exponential increase term must equal to 0 and thus c_2=0 and d_2=0. Substitution of Eqs. (E9) to (E14) into Eq. (E17), allows the coefficients in Eq. (E17) to be determined as a function of λ_i. Since θ_0 in Eq. (E5) is the angle of rotation at x=–L_b under unit moment applied (i.e. θ_0=y'(–L_b)), with dL_b=–da:

$$\frac{d\theta_0}{da} = -\frac{d\theta_0}{dL_b} = \frac{d\left[\frac{dy}{dx}(-L_b)\right]}{dL_b}. \tag{E18}$$

Now, only λ_i with λ_i^4=k_i /(4D_i) is left to be found. As the inset is considered to be ~10^3 times stiffer than the thin compliant layer, the bending rigidity of segment 1 can be approximated as D_1=bE_s*(H–h)^3/12 with the neutral axis passing through the center of the inset. The elastic foundation stiffness, k_i, must also be defined. Kanninen (1973) suggests considering the material between neutral axis of the DCB as an effective spring, which results in $k = 2bE^*/H$ for a homogenous DCB. However, various coefficients other than 2 have been used to calculate k based on FE results for a homogenous DCB (Li et al., 2004; Thouless, 2018), thus it can be used a fitting parameter to match beam theory and a more accurate model. For the beam we considered here, as shown in Fig. E1, segment 2 is homogenous and we take k_2=$2bE_c$*/H. For segment 1, the stiffness of elastic foundation is determined by the stiffness of the material below neutral axis, k_s, and the stiffness of the thin compliant layer, k_c. The stiffness k_s, can be found as k_s=$2bE_s$*/(H-h), similar to previous work. For k_c, the compliant layer studied in this work is a long and slender strip connected to a much stiffer material and in a plane strain condition, thus it is highly confined and has a Poisson's ratio close to 0.5, resulting in k_c=$4bE_c$*/h. They can be treated as springs in series, 1/k_1=1/k_s+1/k_c, to obtain the foundation stiffness:

$$\frac{1}{k_1} = \frac{H-h}{2bE_s^*} + \frac{h}{4bE_c^*}, \tag{E19}$$

Fig. E2 shows the moment as a function of crack front position for DCB containing single long rectangular insets calculated using FE and beam theory (BT) with root rotation represented by the elastic foundation model above. There is reasonable agreement between the two models, but the discrepancy increases as h/H increases. This confirms that the transition near back of the inset can be captured by the elastic foundation model with the assumptions noted above works best for small h/H. The back transition length, L_{back}, which is the distance from crack front position where the moment is 95% of beam theory-predicted critical moment to the back edge of the inset, can be estimated. Note that L_{back} is also the minimum length for the deflection to decay to a negligible value at back edge of the inset so there is negligible end effect from the compliant material behind. From Eq. (E17), the solution can be rescaled with x^*=$\lambda_i x$, thus the critical length L_{back} should also scales with L_{back}^*=$\lambda_i L_{back}$, thus

$$L_{back} \propto \sqrt[4]{\frac{4D}{k}}. \tag{E20}$$

This suggests that a higher D/k leads to a larger L_{back}, which means a longer portion of the inset containing region ahead of the crack front is deformed and the stress is distributed over large area.

Appendix F

Effective bending rigidity of the beam

Effective bending rigidity of the beam (D^*_{eff}) predicted by Euler beam theory can be calculated by regarding one period of the composite beam as two connected beam segments:

$$\frac{L+S}{D_{eff}} = \frac{L}{D} + \frac{S}{D_0}, \tag{F1}$$

Thus

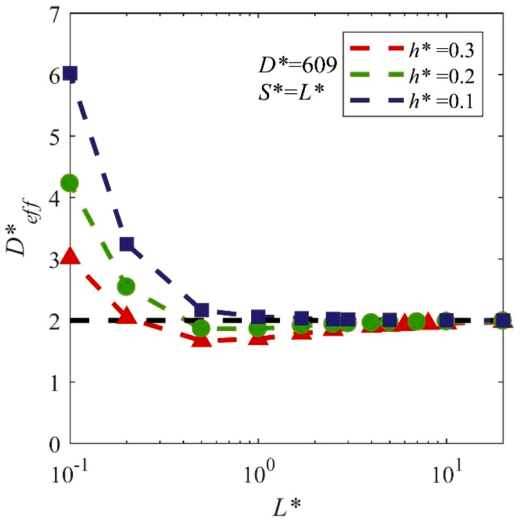

Fig. F1. Effective bending rigidity (D^*_{eff}) of the beam for various L^* and h^* with L^*=S^* (with constant bending rigidity D^*=609 in the inset region) ($M^*_{max}/D^{*1/2}_{eff}$ predicted by Euler beam theory based on Eq. (F4) is shown as dashed black curve).

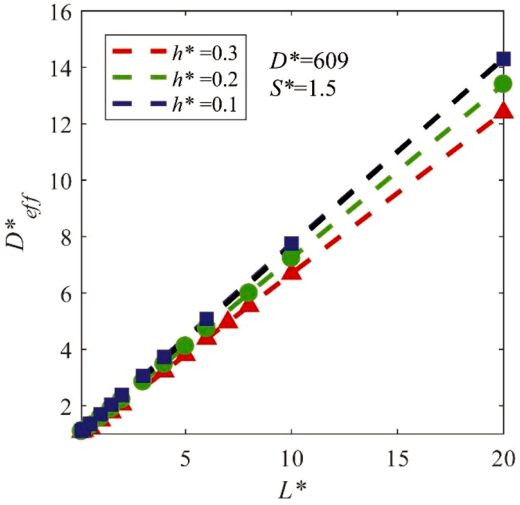

Fig. F2. Effective bending rigidity (D^*_{eff}) of the beam for various L^* and h^* with S^*=1.5 (with constant bending rigidity D^*=609 in the inset region) ($M^*_{max}/D^{*1/2}_{eff}$ predicted by Euler beam theory based on Eq. (F4) is shown as dashed black curve, and it collapsed with the dashed blue curve).

$$D_{eff} = \frac{DD_0(L+S)}{LD_0 + SD}. \tag{F2}$$

For highly-mismatched cases investigated in this paper ($D>>D_0$), Eq. (F2) can be simplified to

$$D_{eff} = \left(1 + \frac{L}{S}\right) D_0, \tag{F3}$$

With D^*_{eff}=D_{eff}/D_0:

$$D^*_{eff} = 1 + \frac{L^*}{S^*}, \tag{F4}$$

Eq. (F4) provides a simple estimation of the effective bending rigidity of the segmented composite beam based on Euler beam theory.

The effective bending rigidity of the beam (D^*_{eff}) calculated from FE are summarized below:

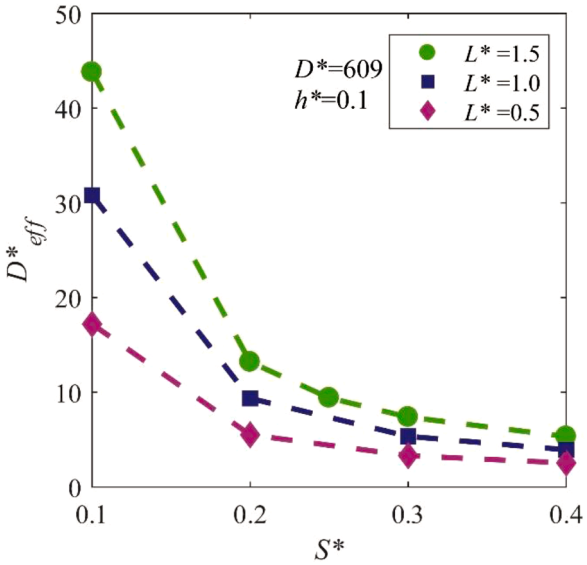

Fig. F3. Effective bending rigidity (D^*_{eff}) of the beam for various L^* and S^* with h^*=0.1 (with constant bending rigidity D^*=609 in the inset region).

References

Anderson, T.L., 2017. Fracture Mechanics: Fundamentals and Applications, Fourth Edition. CRC Press.

Balijepalli, R.G., Fischer, S.C.L., Hensel, R., McMeeking, R.M., Arzt, E., 2017. Numerical study of adhesion enhancement by composite fibrils with soft tip layers. J. Mech. Phys. Solids 99, 357–378. https://doi.org/10.1016/j.jmps.2016.11.017.

Bartlett, M.D., Croll, A.B., King, D.R., Paret, B.M., Irschick, D.J., Crosby, A.J., 2012. Looking beyond fibrillar features to scale gecko-like adhesion. Adv. Mater. 24, 1078–1083. https://doi.org/10.1002/adma.201104191.

Benvidi, F.H., Bacca, M., 2021. Theoretical limits in detachment strength for axisymmetric bi-material adhesives. arXiv Prepr. arXiv:2102.11324.

Carlson, A., Kim-Lee, H.J., Wu, J., Elvikis, P., Cheng, H., Kovalsky, A., Elgan, S., Yu, Q., Ferreira, P.M., Huang, Y., Turner, K.T., Rogers, J.A., 2011. Shear-enhanced adhesiveless transfer printing for use in deterministic materials assembly. Appl. Phys. Lett. 98, 264104 https://doi.org/10.1063/1.3605558.

Crosby, A.J., Shull, K.R., Lakrout, H., Creton, C., 2000. Deformation and failure modes of adhesively bonded elastic layers. J. Appl. Phys. 88, 2956–2966. https://doi.org/10.1063/1.1288017.

Dumont, D., Deschamps, A., Brechet, Y., 2003. On the relationship between microstructure, strength and toughness in AA7050 aluminum alloy. Mater. Sci. Eng. A 356, 326–336. https://doi.org/10.1016/S0921-5093(03)00145-X.

Evans, A.G., McMeeking, R.M., 1986. On the toughening of ceramics by strong reinforcements. Acta Metall. 34, 2435–2441. https://doi.org/10.1016/0001-6160(86)90146-X.

Firouzeh, A., Paik, J., 2017. Grasp mode and compliance control of an underactuated origami gripper using adjustable stiffness joints. IEEE/ASME Trans. Mechatronic. 22, 2165–2173. https://doi.org/10.1109/TMECH.2017.2732827.

Fischer, S.C.L., Arzt, E., Hensel, R., 2017. Composite pillars with a tunable interface for adhesion to rough substrates. ACS Appl. Mater. Interfaces 9, 1036–1044. https://doi.org/10.1021/acsami.6b11642.

Gere, J., Goodno, B., 2009. Mechanichs of Materials, 8th ed. Cengage Learning.

Gludovatz, B., Hohenwarter, A., Catoor, D., Chang, E.H., George, E.P., Ritchie, R.O., 2014. A fracture-resistant high-entropy alloy for cryogenic applications. Science 345, 1153–1158. https://doi.org/10.1126/science.1254581.

Hossain, M.Z., Hsueh, C.J., Bourdin, B., Bhattacharya, K., 2014. Effective toughness of heterogeneous media. J. Mech. Phys. Solids 71, 15–32. https://doi.org/10.1016/j.jmps.2014.06.002.

Hsueh, C.J., Avellar, L., Bourdin, B., Ravichandran, G., Bhattacharya, K., 2018. Stress fluctuation, crack renucleation and toughening in layered materials. J. Mech. Phys. Solids 120, 68–78. https://doi.org/10.1016/j.jmps.2018.04.011.

Hwang, D.G., Trent, K., Bartlett, M.D., 2018. Kirigami-inspired structures for smart adhesion. ACS Appl. Mater. Interfaces 10, 6747–6754. https://doi.org/10.1021/acsami.7b18594.

Ilievski, F., Mazzeo, A.D., Shepherd, R.F., Chen, X., Whitesides, G.M., 2011. Soft robotics for chemists. Angew. Chem. Int. Ed. 50, 1890–1895. https://doi.org/10.1002/anie.201006464.

Jiang, Y., Hor, J.L., Lee, D., Turner, K.T., 2018. Toughening nanoparticle films via polymer infiltration and confinement. ACS Appl. Mater. Interfaces 10, 44011–44017. https://doi.org/10.1021/acsami.8b15027.

Kanninen, M.F., 1973. An augmented double cantilever beam model for studying crack propagation and arrest. Int. J. Fract. 9, 83–92. https://doi.org/10.1007/BF00035958.

Kendall, K., 1975. Control of cracks by interfaces in composites. Proc. R. Soc. Lond. A Math. Phys. Sci. 341, 409–428. https://doi.org/10.1098/rspa.1975.0001.

Kendall, K., 1973. An adhesion paradox. J. Adhes. 5, 77–79. https://doi.org/10.1080/00218467308078440.

Khaderi, S.N., Fleck, N.A., Arzt, E., McMeeking, R.M., 2015. Detachment of an adhered micropillar from a dissimilar substrate. J. Mech. Phys. Solids 75, 159–183. https://doi.org/10.1016/j.jmps.2014.11.004.

Kim, S., Carlson, A., Cheng, H., Lee, S., Park, J.K., Huang, Y., Rogers, J.A., 2012. Enhanced adhesion with pedestal-shaped elastomeric stamps for transfer printing. Appl. Phys. Lett. 100, 171909 https://doi.org/10.1063/1.4706257.

Kolednik, O., Predan, J., Fischer, F.D., Fratzl, P., 2011. Bioinspired design criteria for damage-resistant materials with periodically varying microstructure. Adv. Funct. Mater. 21, 3634–3641. https://doi.org/10.1002/adfm.201100443.

Li, S., Wang, J., Thouless, M.D., 2004. The effects of shear on delamination in layered materials. J. Mech. Phys. Solids 52, 193–214. https://doi.org/10.1016/S0022-5096(03)00070-X.

Luo, A., Mohammadi Nasab, A., Tatari, M., Chen, S., Shan, W., Turner, K.T., 2020. Adhesion of flat-ended pillars with non-circular contacts. Soft Matter 16, 9534–9542. https://doi.org/10.1039/d0sm01105c.

Luo, A., Turner, K.T., 2021. Achieving enhanced adhesion through optimal stress distributions. J. Mech. Phys. Solids 104610.

Luo, A., Turner, K.T., 2020. Mechanics of crack path selection in microtransfer printing: challenges and opportunities for process control. J. Mech. Phys. Solids 143, 104066. https://doi.org/10.1016/j.jmps.2020.104066.
Maugis, D., 2000. Contact, Adhesion, and Rupture of Elastic Solids. Springer Science & Business Media.
Meitl, M.A., Zhu, Z.T., Kumar, V., Lee, K.J., Feng, X., Huang, Y.Y., Adesida, I., Nuzzo, R.G., Rogers, J.A., 2006. Transfer printing by kinetic control of adhesion to an elastomeric stamp.pdf. Nat. Mater. 5, 33–38.
Minsky, H.K., Turner, K.T., 2017. Composite microposts with high dry adhesion strength. ACS Appl. Mater. Interfaces 9, 18322–18327. https://doi.org/10.1021/acsami.7b01491.
Minsky, H.K., Turner, K.T., 2015. Achieving enhanced and tunable adhesion via composite posts. Appl. Phys. Lett. 106, 201604 https://doi.org/10.1063/1.4921423.
Mosadegh, B., Polygerinos, P., Keplinger, C., Wennstedt, S., Shepherd, R.F., Gupta, U., Shim, J., Bertoldi, K., Walsh, C.J., Whitesides, G.M., 2014. Pneumatic networks for soft robotics that actuate rapidly. Adv. Funct. Mater. 24, 2163–2170. https://doi.org/10.1002/adfm.201303288.
Peisker, H., Michels, J., Gorb, S.N., 2013. Evidence for a material gradient in the adhesive tarsal setae of the ladybird beetle Coccinella septempunctata. Nat. Commun. 4, 1607–1608. https://doi.org/10.1038/ncomms2576.
Scholz, I., Baumgartner, W., Federle, W., 2008. Micromechanics of smooth adhesive organs in stick insects: pads are mechanically anisotropic and softer towards the adhesive surface. J. Comp. Physiol. A Neuroethol. Sens. Neural Behav. Physiol. 194, 373–384. https://doi.org/10.1007/s00359-008-0314-6.
Studart, A.R., 2013. Biological and bioinspired composites with spatially tunable heterogeneous architectures. Adv. Funct. Mater. 23, 4423–4436. https://doi.org/10.1002/adfm.201300340.
Thouless, M.D., 2018. Shear forces, root rotations, phase angles and delamination of layered materials. Eng. Fract. Mech. 191, 153–167. https://doi.org/10.1016/j.engfracmech.2018.01.033.
Tuan, W.H., Brook, R.J., 1990. The toughening of alumina with nickel inclusions. J. Eur. Ceram. Soc. 6, 31–37. https://doi.org/10.1016/0955-2219(90)90032-B.
Wang, N., Xia, S., 2017. Cohesive fracture of elastically heterogeneous materials: an integrative modeling and experimental study. J. Mech. Phys. Solids 98, 87–105. https://doi.org/10.1016/j.jmps.2016.09.004.
Wang, W., Ahn, S.H., 2017. Shape memory alloy-based soft gripper with variable stiffness for compliant and effective grasping. Soft Robot. 4, 379–389. https://doi.org/10.1089/soro.2016.0081.
Wang, Z., Xiang, C., Yao, X., Le Floch, P., Mendez, J., Suo, Z., 2019. Stretchable materials of high toughness and low hysteresis. Proc. Natl. Acad. Sci. U. S. A. 116, 5967–5972. https://doi.org/10.1073/pnas.1821420116.
Williams, J.G., 1989. End corrections for orthotropic DCB specimens. Compos. Sci. Technol. 35, 367–376. https://doi.org/10.1016/0266-3538(89)90058-4.
Xia, S., Ponson, L., Ravichandran, G., Bhattacharya, K., 2012. Toughening and asymmetry in peeling of heterogeneous adhesives. Phys. Rev. Lett. 108, 196101 https://doi.org/10.1103/PhysRevLett.108.196101.
Xia, S.M., Ponson, L., Ravichandran, G., Bhattacharya, K., 2013. Adhesion of heterogeneous thin films - I: elastic heterogeneity. J. Mech. Phys. Solids 61, 838–851. https://doi.org/10.1016/j.jmps.2012.10.014.
Zhou, X., Majidi, C., O'Reilly, O.M., 2015. Soft hands: an analysis of some gripping mechanisms in soft robot design. Int. J. Solids Struct. 64, 155–165. https://doi.org/10.1016/j.ijsolstr.2015.03.021.